This is the peer-reviewed, final accepted version for American Mineralogist, published by the Mineralogical Society of America.
The published version is subject to change. Cite as Authors (Year) Title. American Mineralogist, in press.
DOI: https://doi.org/10.2138/am-2023-8985. http://www.minsocam.org/

Revision 1: Ilmenite phase transformations in suevite from the Ries impact structure (Germany) record evolution in pressure, temperature, and oxygen fugacity conditions

Fabian Dellefant[1*] · Claudia A. Trepmann[1] · Wolfang W. Schmahl[1,2] · Stuart A. Gilder[1] · Iuliia V. Sleptsova[1] · Melanie Kaliwoda[1,2]

[1]Department of Earth and Environmental Sciences, Ludwig-Maximilians-University, Theresienstr. 39, 80333 Munich

[2]Mineralogical State Collection Munich (MSM), SNSB (natural science collections of Bavaria), Theresienstr. 39, 80333 Munich

*Corresponding author: fabian.dellefant@lmu.de

Abstract Aggregates of ilmenite with varying amounts of rutile, ferropseudobrookite, and pseudorutile in suevites from the Ries impact structure have been analyzed by light microscopy, analytical scanning electron microscopy, electron microscope analysis, and Raman spectroscopy to constrain their formation conditions. The 10s-100s µm aggregates comprise isometric ilmenite grains up to 15 µm in diameter that form a foam structure (i.e., smoothly curved grain boundaries and 120° angles at triple junctions). Grains with foam structure show no internal misorientations, indicating a post-impact formation. In contrast, ilmenite grains with internal misorientation occurring in the core of the aggregates are interpreted as shocked remnant ilmenite originating from the target gneisses. They can contain twin lamellae that share a common $\{11\bar{2}0\}$ plane with the host and the *c-axis* is oriented at an angle of 109° to that of the host. Similarly, the new grains with foam structure display up to three orientation domains, sharing one common $\{11\bar{2}0\}$ plane for each pair of domains and *c*-axes at angles of 109° and 99°, respectively. This systematic

orientation relationship likely reflects a cubic supersymmetry resulting from the transformation of the initial ilmenite upon shock (>16 GPa) to a transient perovskite-type high-pressure phase (liuite), subsequent retrograde transformation to the polymorph wangdaodeite, and then back-transformation to ilmenite. Whereas the new grains with foam structure formed from complete transformation, the twin domains in the shocked ilmenite are interpreted to represent only partial transformation. Ferropseudobrookite occurs mostly near the rim of the aggregates. An intergrowth of ferropseudobrookite, ilmenite, and rutile as well as magnetite or rarely armalcolite occurs at contact with the (devitrified) matrix. The presence of ferropseudobrookite indicates high temperature (>1140°C) and reducing conditions. The surrounding matrix provided Mg^{2+} to form the ferropseudobrookite-armalcolite solid solution. Rutile can occur within the aggregates and/or along the ilmenite boundaries; it is interpreted to have formed together with iron during the decomposition of ilmenite at lower temperatures (850°-1050°C). We suggest magnetite in the rims formed by electrochemical gradients driven by the presence of a reducing agent, where Fe^{2+} within ilmenite diffused towards the rim. Subsequent cooling under oxidizing conditions led to the formation of magnetite from the iron-enriched rim as well as pseudorutile around ilmenite grains.

Our study demonstrates that the specific crystallographic relationships of ilmenite grains with foam structure indicate a back-transformation from high (shock) pressures >16 GPa; moreover, the presence of associated Fe-Ti oxides helps indicate local temperature and oxygen fugacity conditions.

Keywords

ilmenite shock effects; transformation twinning; liuite; wangdaoedeite; ferropseudobrookite; armalcolite

Introduction

Ilmenite ($Fe^{2+}TiO_3$) is a common Fe-Ti-bearing opaque mineral in magmatic and metamorphic rocks. Its deformation and transformation to ferrimagnetic phases during impact cratering can change the magnetic properties of impactites (e.g., El Goresy 1964; El Goresy et al. 2010; Dellefant et al. 2022), which in turn can result in large-scale magnetic anomalies in impact structures (Pilkington and Grieve 1992; Scott et al. 1997; Plado et al. 1999; Pilkington and Hildebrand 2000; Ugalde et al. 2005; Pohl et al. 2010). Heating of ilmenite under oxidizing conditions leads to the formation of hematite (Fe_2O_3), rutile (TiO_2), and nFe_2O_3 x $nTiO_2$ from 500°-800°C, whereas a complete transformation of ilmenite to pseudobrookite (Fe_2TiO_5) occurs at temperatures above 800°C (Fu et al. 2010). Pseudorutile ($Fe^{3+}{}_2Ti_3O_9$) forms as a transitional phase from ilmenite alteration towards rutile (Teufer and Temple 1966), commonly observed under high oxygen fugacity and below 700°C (Gupta et al. 1991) in combination with iron removal by a leaching agent, such as water, along grain boundaries (Mücke and Bhadra Chaudhuri 1991) and/or structural discontinuities within the grain (Temple 1966; Grey and Reid 1975).

Under reducing conditions, ilmenite dissociates to elemental iron and rutile at temperatures ranging from 850° to 1050°C (Taylor et al. 1972) and forms ferropseudobrookite ($Fe^{2+}Ti_2O_5$) at >1140°C (Lindsley 1965; Keil et al. 1970; Tuthill and Sato 1970; Sargeant et al. 2020), which is mostly found in extraterrestrial material (Keil et al. 1970; Fujimaki et al. 1981). Armalcolite [$(Fe^{2+},Mg)Ti_2O_5$] can be formed from ferropseudobrookite when part of Fe^{2+} is substituted by

Mg^{2+} (Anderson et al. 1970). High-temperature experiments with reducing agents can produce a rim of pure iron around ilmenite grains (Gupta et al. 1990; Zhao and Shadman 1990) with various amounts of rutile, ilmenite, and elemental iron (Gupta et al. 1990; Kucukkaragoz and Eric 2006; Sargeant et al. 2020). Ilmenite is reduced with carbon in an argon atmosphere at 1000°C, resulting in Ti-oxides and finely distributed iron within the core and a rim of metallic iron (Gupta et al. 1990), as well as in veinlets of Ti-oxides within the grain as similarly reported by H_2-reduced ilmenites (Sargeant et al. 2020). Experiments of synthetic ilmenite under reducing conditions with CO between 900 and 1100°C resulted in a core of ilmenite encompassed by an inner rim of rutile and an outer rim of pure iron (Zhao and Shadman 1990). The formation of the iron-enriched rim is attributed to the migration of iron to the grain boundaries (Zhao and Shadman 1990; Kucukkaragoz and Eric 2006), whereas finely distributed iron within the grain is interpreted by a movement of a reducing agent into and out of the grain (Li et al. 2012; Dang et al. 2015; Sargeant et al. 2020).

Liu (1975) described a high-pressure phase transition of ilmenite to an orthorhombic perovskite structure at 14 GPa at 1400-1800°C based on X-ray diffraction data. Furthermore, Leinenweber et al. (1991) documented an unquenchable, high-pressure polymorph of ilmenite with a perovskite structure forming at 16 GPa and ≈27°C using a diamond-anvil cell and in-situ powder diffraction. Upon decompression, the high-pressure phase transformed into a meta-stable $FeTiO_3$ phase with a lithium niobate structure (Mehta et al. 1994). Further studies documented these high-pressure phase transitions as a function of temperature [7-10 GPa at 1327-1527°C (Mehta et al. 1994); 10-20 GPa at ≈400°C (Ming et al. 2006); 20-30GPa at ≈1337°C (Nishio-Hamane et al. 2012)]. The orthorhombic perovskite-type $FeTiO_3$ phase named liuite was reported by Ma and Tschauner (2018) from the Shergotty martian meteorite. Xie et al. (2020) described a natural occurrence of the lithium niobate-type $FeTiO_3$ named wangdaodeite from the Suizhou L6

This is the peer-reviewed, final accepted version for American Mineralogist, published by the Mineralogical Society of America.
The published version is subject to change. Cite as Authors (Year) Title. American Mineralogist, in press.
DOI: https://doi.org/10.2138/am-2023-8985. http://www.minsocam.org/

chondrite. Wangdaodeite was reported for the first time in naturally occurring rocks from Zipplingen in the Ries impact structure by Tschauner et al. (2020).

Further shock experiments with pressures ranging from 23 to 53 GPa reported quenchable orthorhombic Fe_2TiO_4 (Hashishin et al. 2014), Fe_2TiO_4 (Ca_2TiO_4-Type) + TiO_2 and wüstite (FeO) + TiO_2 (Nishio-Hamane et al. 2012), wüstite and orthorhombic $FeTi_3O_7$ (Nishio-Hamane et al. 2010), as well as $Fe_{1-\delta}Ti_\delta O$ and $Fe_{1+\delta}Ti_{2-\delta}O_\delta$ (Wu et al. 2009). Based on hybrid-density functional modelling, Wilson et al. (2005) predicted a phase transition of $FeTiO_3$ above 65 GPa to TiO_2 (cotunnite) + FeO (wüstite).

Studies of ilmenite shock effects in ilmenite from natural impactites, however, are relatively scarce (Minkin and Chao 1971; Sclar et al. 1973; Syono et al. 1981; Tschauner et al. 2020; Dellefant et al. 2022). This study aims to shed light on the potential of ilmenite as a recorder of temperature, pressure, and oxygen fugacity conditions in impactites based on microfabric and phase relation analyses. To this aim, we investigated 35 ilmenite aggregates within suevites from the Ries impact structure (Zipplingen and Aumühle) with optical light microscopy (transmitted and reflected), Raman spectroscopy, and scanning electron microscopy (SEM) in combination with electron backscatter diffraction (EBSD), as well as electron microprobe (EMP) measurements.

Geological overview

The ≈26 km diameter Ries impact structure formed about 14.8 Ma ago (Rocholl et al. 2017, 2018; Schmieder et al. 2018a, 2018b; Schwarz et al. 2020; Di Vincenzo 2022). The Ries impactor hit a 600-700 m thick, sedimentary layer of limestones, shales, and sandstones that overlay Variscan

basement (Bolten and Müller 1969; Pohl et al. 1977) mainly composed of various paragneisses, amphibolites, and metagranites (Schmidt-Kaler 1969; Pohl et al. 1977; Hüttner and Schmidt-Kaler 1999; Stöffler et al. 2013). The Ries structure can be divided into the inner crater, the inner wall [being presumably the rim of the primary inner crater, (Wünnemann et al. 2005)], the megablock zone, and the outer crater rim (Stöffler et al. 2013). Suevite constitutes the most important ejecta blanket that contains polymict impact breccia bearing both lithic clasts and cogenetic melt particles (Stöffler and Grieve 2007; Stöffler et al. 2013). On a microscopic scale, (devitrified) glass represents a heterogeneous distribution of incompletely mixed melts of different compositions interspersed with vesicles indicating gas phases (von Engelhardt et al. 1995). Based on the occurrence of high-temperature phases such as baddeleyite + SiO_2 formed from zircon, fused SiO_2 formed from quartz, or pseudobrookite and rutile formed from ilmenite (El Goresy and Chao 1976), von Engelhardt et al. (1995) suggested the initial melt temperature exceeded 2000°C. Glass fragments in suevites were reported to contain ilmenite with accompanying rutile, magnetite, and pseudobrookite (El Goresy 1964), as well as armalcolite and polycrystalline ilmenite (El Goresy and Chao 1976).

Here, we studied ilmenite aggregates in suevite from a small outcrop between the outer and inner ring in the northwestern part of the Ries impact structure, close to the village of Zipplingen (sample CT827a, Lat 48.92615°, Long 10.40889°) and in a shocked gneiss clast within suevite sampled close to the contact of the underlying bunte breccia in the Aumühle quarry at the northeastern rim of the structure (sample R20-16A, Lat 48.97151°, Long 10.62908°).

Methods

Uncovered and polished thin sections (25 µm) were prepared from the samples and investigated by polarization microscopy (Leica DM2700 P) using both reflected and transmitted light. Photomicrographs were taken with a Leica MC170 HD camera and processed with the Leica Application Suite X 3.08.19082 software.

In-situ micro-Raman spectroscopy was carried out at the Mineralogical State Collection Munich (SNSB) to identify the iron-bearing phases with a HORIBA JOBIN YVON XploRa ONE system. The Raman spectrometer is equipped with a Peltier-cooled CCD detector and edge filters. An 1800g/mm grating was used in combination with a 532 nm 2ω-Nd:YAG laser on iron-bearing phases in an attenuated mode (10% laser power) corresponding to max. 0.9 mW on the sample surface to avoid oxidation (Bauer et al. 2011; Kaliwoda et al. 2021), which could transform magnetite to hematite thereby leading to a false phase determination. Hole and slit diameters were 300 µm and 100 µm, respectively, using an integration time of 2 x 16 s. On the sample surface, a 100x long working distance objective resulted in a 0.9 µm laser spot size. Wavelength calibration was conducted with a pure Si-wafer chip on the predominant 520±1 cm^{-1} peak. The precision in the Raman peak position is estimated at ±1.5 cm^{-1}.

The samples were studied with a Hitachi SU5000 SEM, equipped with a NordlysNano high-sensitivity EBSD detector (Oxford Instruments), energy-dispersive X-ray spectroscopy (EDS) detector (Oxford Instruments), field emission gun, as well as backscattered electron (BSE) and secondary electron (SE) detectors at the Department for Earth and Environmental Sciences, LMU Munich. Thin sections were chemo-mechanically polished with a colloidal silicon suspension (Syton) for EBSD to reduce the surface damage produced from preparation. SEM observations used accelerating voltages of 20 kV and a working distance ranging from 10 to 25 mm. The sample holder was tilted at 70° with respect to the electron beam. EBSD patterns were acquired

and automatically indexed with the AZtec analysis software 4.2 (Oxford Instruments). Step sizes for automatic mapping were between 0.5 µm and 2 µm, depending on the resolution and the desired EBSD-pattern quality. EBSD data were processed by the Channel software 5.12.74.0 (Oxford Instruments). The inferred different crystallographic orientations were analyzed by characterizing the smallest angle required to rotate one orientation into another, i.e., by the misorientation angle and the misorientation axis [e.g., Wheeler et al. (2001)]. Grains are detected by a misorientation angle threshold of 10°. Stereograms in the proceeding figures are equal-angle projections of the lower hemisphere with viewing directions identical to the EBSD map.

The chemical compositions of ilmenite, ferropseudobrookite, armalcolite, rutile, and pseudorutile were measured using a Cameca SX-100 electron microprobe (EMP) at the Department for Earth and Environmental Sciences, LMU Munich. As measurement conditions, 15 kV accelerating voltage, 40 nA sample current, and a focused beam were applied. Calibration was performed using silicate and oxide standards: periclase (Mg), albite (Na), bustamite (Mn), Fe_2O_3 (Fe), wollastonite (Ca, Si), rutile (Ti), and orthoclase (K, Al).

Results

Sample description

The investigated suevite sample from Zipplingen (CT827a) consists of ≈85% (devitrified) glass, in which roundish to elongate aggregates of Fe-Ti-oxides with a long axis of 10s to 100s of µm are homogeneously distributed (Fig. 1a, b). The aggregates consist mostly of ilmenite with various amounts of rutile, ferropseudobrookite, and sphene. Magnetite occurs as µm-sized grains dispersed in the matrix and often occurs as a rim around the Fe-Ti-oxide aggregates (Fig. 1a).

Calcite grains (≈15%) can have (devitrified) glass as inclusions (Fig. 1b, yellow arrows) and calcite can be included in (devitrified) glass (Fig. 1b, orange arrows). Irregular phase boundaries of calcite are concave with respect to the glass matrix, where the sharp point of the cusps of the silicate glass-calcite phase boundary points towards the silicate glass (Fig. 1b).

Sample R20-16A from the Aumühle quarry can macroscopically be recognized as a gneiss clast within suevite by its lighter color and foliation. In polarized light, it is characterized by a cryptocrystalline matrix with <10% vesicles (Fig. 1c, d). Elongate ilmenite aggregates with a long axis of several 10s to 100s of μm, as well as secondary hematite, occur homogeneously distributed in the matrix (Fig. 1c). Minerals in the gneiss clast were almost completely amorphized due to the meteorite impact, as evidenced by the cryptocrystalline matrix (Fig. 1d), indicating shock pressures of 35-45 GPa, representing shock stage F-S5 (Stöffler et al. 2018) or II (IUGS system; Stöffler and Grieve 2007).

Phase determination of Fe-Ti-oxides

The Fe-Ti bearing phases in the aggregates were determined by optical reflected light microscopy and confirmed by Raman spectroscopy, chemical EDS and EMP analyses, as well as EBSD patterns. Ilmenite has the main Raman peaks at 227, 333, 371, and 449 cm^{-1} with the prominent peak at 683 cm^{-1} (Fig. 2a) (Wang et al., 2004). The rutile spectra have main Raman peaks at 240, 446, and 611 cm^{-1} (Fig. 2b) (Mazza et al., 2007). Ferropseudobrookite has prominent Raman peaks at 134, 204, 317, and 643 cm^{-1} and a relatively wide peak at 773 cm^{-1} (Fig. 2c), in accordance with spectra of isostructural karooite ($MgTi_2O_5$) (Liermann et al. 2006; He et al. 2017) in combination with a Fe/Ti ratio of ≈1:2 based on EDS and EMP analysis. Peak broadening is associated with a disordered crystal structure (Cynn et al. 1992; Liermann et al.

2006). Magnetite shows typical Raman peaks at 294 and 530 cm^{-1} with the main peak at 661 cm^{-1} (Fig. 2d) (Wang et al., 2004). Within the matrix, magnetite spectra display peaks at 538 and 666 cm^{-1} (Fig. 2e) and thus differ slightly from magnetite at the Fe-Ti-oxide aggregate rim (compare Fig. 2d). We observed additional peaks from the crystallized matrix at 324, 368, and 392 cm^{-1} and a strong peak at 1002 cm^{-1} (Fig. 2e). Sphene displays the main Raman peaks at 166, 254, 335, 468, 548, and 608 cm^{-1} (Fig. 2f) in agreement with Pantić et al. (2014). Within the Aumühle suevite sample (R20-16A), ilmenite has major Raman peaks at 224, 329, 372, and 681 cm^{-1} (Fig. 2g) (Wang et al., 2004). The Raman peaks of pseudorutile are very broad and overlapping, with main peaks at about 153, 264, 312, 419, 557, 599, 693, and 823 cm^{-1} (Fig. 2h) as reported by Imperial et al. (2022).

Microfabrics of ilmenite and associated Fe-Ti-phases in suevite from Zipplingen

Ilmenite within the Zipplingen suevite (CT827a) has a composition ranging from $Fe_{0.88}Mn_{0.08}Mg_{0.06}Ti_{0.98}O_3$ to $Fe_{0.88}Mn_{0.12}Mg_{0.02}Ti_{0.98}O_3$ (Fig. 3a-g; Tab. 1) with small amounts of Al_2O_3. Chemical profiles from the core of the ilmenite aggregate towards the rim conducted with the EMP show an increase in the Fe/Ti ratio (0.83 – 1.03), which correlates with an increase in the Al_2O_3 content (0.07-0.33 wt.%) and a decrease of the analytical total (98.56-96.92 wt.%) (Fig. 3g, h; Tab. S1). The deviation from a total of 100 wt.% of ilmenite can be explained by the presence of a Fe_2O_3 component, which decreases the total wt.% when expressed as FeO. Rutile occurs with variable amounts of FeO (Tab. S1: #1-#4), up to 20 µm in diameter in the cores of the aggregates (Fig. 3a, g) or distributed as µm-sized grains along ilmenite boundaries (Fig. 3c, d). (Sub-)euhedral magnetite grains, <5 µm in diameter, can occur at the rim or within the matrix at a close distance to the ilmenite aggregate (Figs. 3a, c, e, f, 4a).

We distinguish two different types of ilmenite grains in the aggregates based on their internal misorientations, grain shape, and composition (Figs. 3-6): (i) Small, isometric grains of up to 15 µm in diameter show smoothly curved grain boundaries and 120° angles at triple junctions, forming a so-called foam structure (Fig. 3a, b, d). They have generally low internal misorientations with angles <3° (Figs. 4b, c, e, 6b). (ii) In contrast, in the core of the aggregates coarse ilmenite grains can occur that have a short wavelength lamellar internal misorientation with misorientation angles of >10° (Figs. 4 c, d, 5a). These deformed grains can contain a few µm wide twin lamellae that are characterized by a misorientation angle of ≈75° around a misorientation axis parallel to $[\bar{2}110]$, which corresponds to *c-axes* at an angle of ≈109° and a common $\{11\bar{2}0\}$ plane (Fig. 5a, c, e). This crystallographic relationship does not correspond to the known (0001), $\{10\bar{1}1\}$, and $\{10\bar{1}2\}$ twin systems of ilmenite (Minkin and Chao 1971; Sclar et al. 1973; Syono et al. 1981; Dellefant et al. 2022). In some aggregates, only isolated ilmenite grains with internal misorientations are preserved (Fig. 6b, white arrows). The deformed ilmenites have similar crystallographic orientations within single aggregates (Fig. 6e, f).

The ilmenite grains with foam structure and low internal misorientation (Fig. 4a-c, 5a, 6) can show crystallographic orientations scattering largely around that of the deformed ilmenite with internal misorientations (Fig. 4d, e, 5a, c, e, 6). The orientations depict maxima that correspond to the twin relationship, i.e., they share a common $\{11\bar{2}0\}$ plane and *c*-axes that are at an angle of ≈109° (Figs. 5, 6f). Up to three distinct orientation domains were observed with 109° or 99° angles, respectively, between the *c*-axes (Fig. 5b, d, f, 6f). The grains with foam structure can show varying grain sizes (Figs. 5b, 6a, b). Larger grains (>10 µm) are commonly concave and have a high number of neighbors (>6, Fig. 6a, white arrows), and smaller new grains are mostly convex and have fewer neighbors (<6), which suggests some grain boundary migration driven by

the reduction in interfacial free energy, i.e., grain growth (e.g., Nicolas and Poirier, 1976; Evans et al., 2001). Strain-free grains with foam structure can contain minor amounts of alumina (0.02-0.11 wt.%), whereas the deformed grains are alumina-free (Tab. 1).

Ferropseudobrookite occurs at the boundary of the aggregate with the matrix, or along cracks (Fig. 7b-f), and is locally associated with sphene ($CaTi[O|SiO_4]$) (Figs. 7b, c, 8b), with grains diameters of up to 10s of µm in diameter (Figs. 7b-f, 8a, b, d). Ferropseudobrookite displays a symplectitic intergrowth with ilmenite and rutile towards the core of the aggregate (Fig. 7c-e) with random orientations (Fig. 8d, f), whereas ilmenite displays one maximum but also dispersed crystallographic orientations (Fig. 8c, e) and can occur locally as a fine-grained rim around the aggregate (Fig. 8b, c). In contrast to ilmenite, ferropseudobrookite has minor Mn concentrations (Fig. 8b, g). Locally, at the Fe-Ti-oxide boundary towards the matrix, Mg-enrichment indicates compositions within the ferropseudobrookite-armalcolite solid solution ($Fe_{1.02}Mn_{0.04}Mg_{0.13}Ti_{1.79}Si_{0.09}Al_{0.02}Ca_{0.01}Na_{0.01}O_5$; Fig. 8h; Tab. 1). The occurrence of ferropseudobrookite and/or rutile in the aggregates correlates with the presence of µm-sized (sub-)euhedral magnetite at the rim or a close distance within the matrix (Fig. 7f).

Microfabrics of ilmenite and associated Fe-Ti-phases in suevite from Aumühle

Within sample R20-16A from the Aumühle quarry, ilmenite aggregates have an average composition of $Fe_{0.92}Mg_{0.04}Mn_{0.04}TiO_3$, with a very similar polycrystalline microfabric as Zipplingen sample CT827a, possessing a foam structure of single grains up to 15 µm in diameter (Figs. 3a, b, 9a) with intergranular cracks (Fig. 9b). No ferropseudobrookite was detected, instead, pseudorutile can be present as µm-sized rim surrounding single ilmenite grains, as larger crystals with some ilmenite remnants in the core (Fig. 9c, d), or completely replacing ilmenite

with elongated pores exhibiting a preferred orientation (Fig. 9e). A few aggregates have a ≤5 µm wide rim of 0.5 µm x 2µm-sized intergrown ilmenite needles (Fig. 9f).

Distribution of aggregates within the samples

Of 35 ilmenite orientation investigations within aggregates from Zipplingen and Aumühle, three display three distinct maxima with a common $\{11\bar{2}0\}$ plane, eight display two orientation maxima with a common $\{11\bar{2}0\}$ plane, and ten display one weak to moderate maxima, whereas 14 display only dispersed orientations. Three aggregates show coarse irregular ilmenite with short wavelength lamellar misorientations, in two of these aggregates the deformed ilmenites have twin lamellae.

In total, 23 aggregates of Fe- and/or Ti-bearing phases within the Zipplingen suevite (CT827a) were investigated with SEM/EBSD, where ilmenite is always present (Table 2). Aggregates range from 10 µm x 10 µm to 160 µm x 80 µm in size and often show a distinct rim (n=15) comprised of different Fe-Ti-oxides. We observed no size or distribution dependence of aggregates with (10 µm x 10 µm – 160 µm x 80 µm) or without rims (40 µm x 20 µm – 160 µm x 50 µm), as well as no preferred occurrence of distinct phases as a function of size. The aggregates are distributed homogeneously throughout the thin section.

From Aumühle (R20-16A), 12 aggregates of Fe- and/or Ti-bearing phases were investigated with SEM/EBSD where ilmenite was consistently present (Table 3). Aggregates range from 10 µm x 5 µm to 180 µm x 120 µm in size and can display rims (n=4) composed of ilmenite. The aggregates are distributed homogeneously throughout the thin section.

Discussion

Ilmenite grains from Variscan gneisses shocked to low pressure-temperature conditions from the Ries impact structure show neither a comparable foam structure (Figs. 3a, b, 4, 5, 6) nor short wavelength lamellar misorientation patterns, nor twinning (Figs. 4, 5a), as described in this study. The coarse ilmenite with short wavelength lamellar internal misorientation (Figs. 4, 5a) is interpreted to be preserved shocked ilmenites originating from the target gneisses. The strain-free grains with foam structure (Figs. 3a, b, 4, 5) document an equilibrium fabric and some grain growth, which is indicative of isostatic conditions during their formation (e.g., Nicolas and Poirier, 1976; Evans et al. 2001). Therefore, they are interpreted to have formed after the shock event. Possible processes for the formation of the new grains, which will be discussed in the following, might be (i) strain-induced grain boundary migration, i.e., recrystallization of the originally shocked ilmenite, (ii) crystallization from a Fe-Ti-oxide glass or melt formed upon shock loading and unloading or (iii) phase transformations from transient high-pressure phases formed during shock compression.

Similar ilmenite aggregates as those studied here have been found in kimberlite pipes (Pasteris 1980; Haggerty 1991; Kostrovitsky et al. 2020), which were interpreted as having formed from cumulates in the deep mantle that were deformed and recrystallized during ascent to the crust (Frick 1973; Mitchell 1973). Recrystallization, i.e., grain boundary migration driven by the reduction in strain energy, to replace the shocked original ilmenite grain would result in sutured grain boundaries (Drury and Urai 1990), which is rarely observed for some remnant shocked grains (Fig. 6a, b). In contrast, the foam structure indicates that the reduction in interfacial free energy was the driving force for the grain boundary microstructure formation (e.g., Nicolas and Poirier, 1976; Evans et al. 2001). Furthermore, recrystallization cannot explain the specific

crystallographic relationships with up to three distinct orientation maxima with a common $\{11\bar{2}0\}$ plane, comparable to the twin relationship of the shocked remnant grains (Fig. 5b, d, f, 6). Nor can recrystallization explain the occurrences of the different Fe-Ti-phases. The same holds for crystallization of ilmenite grains from a glass or melt. Foam-structured ilmenite aggregates also occur in the suevite sample from Aumühle, which does not display high-temperature phases, such as ferropseudobrookite or pseudobrookite, indicating that temperatures were insufficient for melting.

We suggest that (1) the ilmenite aggregates with foam structure and (2) specific crystallographic relationship similar to the twin relationship in remnant shocked grains, both reflect phase transformations from transient high-pressure phases that were generated upon shock compression and decompression, as discussed below. We then discuss the formation conditions of the other Fe-Ti phases in the aggregates.

Ilmenite transformation twins and associated orientation relationship between new grains

The observed twin lamellae in shocked ilmenite with a misorientation angle of ≈75° around a misorientation axis parallel to $[\bar{2}110]$, and a common $\{11\bar{2}0\}$ plane (Fig. 5a, c, e) has not been reported for ilmenite so far. Shocked ilmenites in nature and laboratory experiments generate (0001), $\{10\bar{1}1\}$, and $\{10\bar{1}2\}$ twins (Minkin and Chao 1971; Sclar et al. 1973; Syono et al. 1981; Dellefant et al. 2022). No similar mechanical twins are observed in our study.

The two observed twin domains (host and lamellae) in Figure 5a, c, e are characterized by an angle of ≈109° between the *c*-axes, i.e., the threefold axes (Fig. 5e); this angle is very close to the value of the tetrahedral angle between threefold axes in the cubic system (109.47°). The threefold

axes of the two twin domains in Figure 5e span a plane which is perpendicular to the apparent interface plane of the host and the twin (Fig. 5a, c, e). The crystallographic preferred orientations of the aggregates with foam structure (Fig. 5f) are characterized by three orientation domains, where the *c*-axes enclose similar angles of 109° and 99°, respectively. Furthermore, each of the three distinct orientation domains shows one common $\{11\bar{2}0\}$ plane with the other two domains, reflecting the same twin operation as in Figure 5a ,c, e that maps any two of the domains onto each other. These characteristics suggest a twinning process related to a cubic supersymmetry: While two of the three orientation domains have a common $\{11\bar{2}0\}$ plane, the deviation from a cubic matrix does not allow a third domain to have a common pole with the other two simultaneously (e.g., Bueble et al. 1998; Hahn and Klapper 2006; Janovec and Přívratská 2006), explaining the 99° angle between the *c*-axes of two of the observed orientation domains. The space group of ilmenite is $R\bar{3}$ (No. 148) (Barth and Posnjak 1934) corresponding to point group $\bar{3}$. A twin operation must not be element of the space- or point group of the twinned phase and the twin operation is, accordingly, not an element of $\bar{3}$. The observed twin operation can be expressed as (a) a 180° rotation around the bisecting angle axis of the c-axes of the twin pair (Fig. 5e) combined with (b) a 180° rotation around the c-axis of one of the twins. Further, combining the $\bar{3}$ point group symmetries of the ilmenite twin domains in their observed mutual orientation with the (a) 180° rotation, leads to a compound supersymmetry equal to the cubic crystallographic point group $m\bar{3}m$ (Fig. 10). The order of point group $m\bar{3}m$ is 48, whereas the order of point group $\bar{3}$ is 6. Therefore, eight (48/6 = 8) equivalent twin domains are theoretically possible. The rhombohedral $\bar{3}$ axis can be chosen along any of the four <111> directions of the cubic compound supersymmetry. Moreover, for each choice of $<111>_{cub}$ direction, there are two choices for the orientation of the $\vec{a}$, $\vec{b}$-axes, since $m\bar{3}m$ also has a threefold rotation axis parallel

This is the peer-reviewed, final accepted version for American Mineralogist, published by the Mineralogical Society of America.
The published version is subject to change. Cite as Authors (Year) Title. American Mineralogist, in press.
DOI: https://doi.org/10.2138/am-2023-8985. http://www.minsocam.org/

to the $\bar{3}$ roto-inversion. In the case of the pole figure shown in Figure 5e, the projection is approximately along a fourfold axis of the supersymmetry group m$\bar{3}$m with only two of the 8 theoretically equivalent twin states realized in the investigated ilmenite grain. In Figure 5f, however, the projection is approximately along a threefold axis of the m$\bar{3}$m compound supersymmetry and three orientation domains out of the 8 possible orientation domains are present. The Bain lattice-correspondence matrix between the rhombohedral and the cubic lattice, expressed for one out of the 8 possibilities is:

$$(\vec{a} \quad \vec{b} \quad \vec{c})_{cub} = (\vec{a} \quad \vec{b} \quad \vec{c})_{hex} \begin{pmatrix} -1/3 & -1/3 & -2/3 \\ +1/3 & -2/3 & -1/3 \\ +1/6 & +1/6 & -1/6 \end{pmatrix} \text{(Eq. 1)}$$

$$(\vec{a} \quad \vec{b} \quad \vec{c})_{hex} = (\vec{a} \quad \vec{b} \quad \vec{c})_{cub} \begin{pmatrix} 1 & 0 & 2 \\ 0 & -1 & 2 \\ 1 & -1 & -2 \end{pmatrix} \text{(Eq. 2)}$$

(the columns of the matrix give the new lattice basis vectors in terms of the old)

Twins where the twin element is a symmetry element of a supergroup $\mathbb{G}$ of the space- or point group $\mathbb{H}$ of the twinned phase are frequent in cases where a phase transition occurs from a high-symmetry phase of symmetry $\mathbb{G}$ (usually at high temperature) to a low-symmetry phase with subgroup symmetry $\mathbb{H}$ of $\mathbb{G}$. They are called transformation twins (Janovec and Přívratská 2006).

A high-pressure polymorph of ilmenite, liuite, with an orthorhombic (space group Pnma, No.62) perovskite structure (Ma and Tschauner 2018) is reported to form at pressures >16 GPa (Liu 1975; Leinenweber et al. 1991). The Pnma perovskite structure results from a simple displacive distortion of the ideal cubic Pm$\bar{3}$m perovskite structure (Fig. 10) as similarly discussed by Wang et al. (1991). Upon decompression, liuite transforms first to wangdaodeite (Xie et al. 2020), which is a meta-stable $FeTiO_3$ with a lithium niobate structure, space group R3c (No.161) (Abrahams et al. 1966; Weis and Gaylord 1985; Mehta et al. 1994; Ma and Tschauner 2018) and

a related generation of transformation twins due to the many symmetry-equivalent ways of forming wangdaodeite from liuite. Moreover, Wangdaodeite finally transforms to ilmenite (space group $R\bar{3}$) with resulting transformation twins reported in ilmenite (Leinenweber et al. 1994; Mehta et al. 1994). Typically, transformation twins result from phase transitions of the displacive or order-disorder type (e.g., Bueble et al. 1998; Hahn and Klapper 2006; Janovec and Přívratská 2006). However, the ilmenite, $LiNbO_3$, and perovskite structure types are topologically different but nevertheless have related unit cell geometries (Fig. 10). Therefore, the observed twins are interpreted as transformation twins generated by phase transitions with some reconstructive character, albeit with a topotactic relationship between the lattices involved. The experimentally observed prograde and retrograde phase transition sequence (Wang et al. 1991; Leinenweber et al. 1994; Mehta et al. 1994) is sketched in Figure 10a. Leinenweber et al. (1994) argued that as a result of the retrograde perovskite-type to $LiNbO_3$-type phase transition, the mirror planes $(100)_{orth}$, $(010)_{orth}$, and $(001)_{orth}$ in the Pnma perovskite point group disappear, with the latter causing the formation of twinning as similarly discussed by Wang et al. (1991). We follow essentially a similar line of argument and extend it by the new information of the 109° angle between the *c*-axes of the twin domains: additionally, it must be considered that the symmetry of the orthorhombic perovskite liuite Pnma (point group mmm) is also a subgroup of the cubic perovskite symmetry $Pm\bar{3}m$ (point group $m\bar{3}m$). Thus, the $m\bar{3}m$ symmetry is a common supergroup of the lattices of all involved phases (Fig. 10b) and becomes the inherent compound symmetry of the twinning process, without an actual cubic perovskite phase necessarily needing to occur during the impact or the retrograde process. Therefore, the transformation from ilmenite to liuite upon shock compression and transformation to wangdaodeite and finally ilmenite upon unloading (Fig. 10) explains the observed twinning in shocked ilmenite and orientation relationship of new grains in our EBSD maps.

This is the peer-reviewed, final accepted version for American Mineralogist, published by the Mineralogical Society of America.
The published version is subject to change. Cite as Authors (Year) Title. American Mineralogist, in press.
DOI: https://doi.org/10.2138/am-2023-8985. http://www.minsocam.org/

Wangdaodeite has recently been detected in gneiss inclusions within suevites from Zipplingen, the same locality as our samples, where the documented BSE images of Tschauner et al. (2020, Fig. 1b) show similar microstructures, as those analyzed here (Figs. 3, 7, 8a). However, with Raman spectroscopy, we did not detect wangdaodeite as there was no indication of the characteristic peak of 739±1 cm^{-1} compared to the Raman spectrum of ilmenite (Xie et al. 2020). The metastability of naturally occurring wangdaodeite in the Ries structure was suggested by Tschauner et al. (2020) due to doping of a few mol.% of $MnTiO_3$, which increases the kinetic barrier for a back-transformation to ilmenite. In contrast to the ilmenite-wangdaodeite-bearing gneiss inclusions investigated by the latter authors, our sample is comprised of ilmenites within a (devitrified) glass matrix indicating higher temperatures, which could favor the back-transformation to ilmenite despite a few mol.% of $MnTiO_3$ being present (Fig. 8h; Tab. 1).

Similar microstructures as observed in our study have been documented within shocked zircons, where the high-pressure phase reidite occurs as lamellae or, with increasing shock pressures, replaces the entire grain. For the latter, back-transformation to μm-sized granular zircon leads to a systematic orthogonal disorientation relationship of ≈90° around <110> directions between adjacent granules, topotactically controlled by the crystallographic structure of the reidite, leading to a similar orientation relationship of the metastable reidite lamellae and the host zircon (Erickson et al. 2017; Timms et al. 2017; Cavosie et al. 2018). Similarly, the foam structure of ilmenite with distinct orientation maxima of the crystallographic orientations of ilmenite grains can be used as a geobarometer to indicate pressure conditions >16 GPa realized for example in impactites and kimberlites.

Ferropseudobrookite and armalcolite formation conditions

This is the peer-reviewed, final accepted version for American Mineralogist, published by the Mineralogical Society of America.
The published version is subject to change. Cite as Authors (Year) Title. American Mineralogist, in press.
DOI: https://doi.org/10.2138/am-2023-8985. http://www.minsocam.org/

Ferropseudobrookite ($Fe^{2+}Ti_2O_5$) requires >1140°C and a low oxygen fugacity to form (Lindsley 1965; Keil et al. 1970; Tuthill and Sato 1970; Sargeant et al. 2020). In contrast, ferrous-ferric pseudobrookite solid solution forms >800°C under oxidizing conditions (Fu et al. 2010). Therefore, in the Zipplingen sample (CT827; Figs. 7c-f, 8b, d), we interpret that the ferropseudobrookite at the boundary of the Fe-Ti-oxide near the matrix, representing quenched melt, formed from ilmenite as a result of shock-heating after shock-unloading at >1140°C and low oxygen fugacity according to:

$$2FeTiO_3 \rightarrow FeTi_2O_5 + FeO \quad \text{(Eq. 3)}$$

Maximum temperatures could have exceeded the FeO-TiO_2 melting point of ≈1400°C (Eriksson and Pelton 1993) locally at the aggregate boundary towards the silicate melt. However, the foam structure of ilmenite grains with specific crystallographic relationship documents that solid-state phase transformations dominated.

Armalcolite [$(Fe^{2+},Mg)Ti_2O_5$] is stable above 1010±20°C at ambient pressure (Lindsley et al. 1974) with a pseudobrookite structure (Bowles 1988). Armalcolite was first documented in lunar samples from the Apollo 11 (Anderson et al. 1970) and Apollo 17 missions (Haggerty 1973; El Goresy et al. 1974) and later on Earth in kimberlites (e.g., Haggerty 1975) and lower crustal / mantle xenoliths (e.g., Grégoire et al. 2000; Hayob and Essene 1995; Spiridonov et al. 2019). El Goresy and Chao (1976) first described the occurrence of armalcolite and associated ilmenite in the Ries impact structure within glasses in suevite from diverse localities based on FeO/MgO of 21.1 to 4.5. Microscopic observation and microprobe data of a rutile core and an armalcolite rim suggest a reaction of pre-existing rutile and silicate melt (El Goresy and Chao 1976). In our study, chemical interaction of the silicate melt, represented by the (devitrified) matrix with the Fe-Ti-oxide aggregates, presumably led to the formation of a rim of Mg-bearing

This is the peer-reviewed, final accepted version for American Mineralogist, published by the Mineralogical Society of America.
The published version is subject to change. Cite as Authors (Year) Title. American Mineralogist, in press.
DOI: https://doi.org/10.2138/am-2023-8985. http://www.minsocam.org/

454 ferropseudobrookite-armalcolite solid solution formed from ilmenite (Fig. 8a, b, d, f, h), as also
455 suggested by El Goresy and Chao (1976):

456 $$2(Fe,Mg)TiO_3 \rightarrow (Fe,Mg)Ti_2O_5 + FeO \quad \text{(Eq. 4)}$$

457 An interaction of ferropseudobrookite with the surrounding silicate melt, where the latter
458 provides MgO in exchange for FeO could also produce armalcolite:

459 $$FeTi_2O_5 + MgO \rightarrow (Fe,Mg)Ti_2O_5 + FeO \quad \text{(Eq. 5)}$$

460 In each case, FeO would be enriched within the silicate melt close to the Fe-Ti-oxide aggregates.
461 Temperature stability experiments found that armalcolite decomposes unless rapidly quenched
462 (Lindsley et al. 1974). Adjacent to the Fe-Ti-oxide aggregate and within fractures, sphene can be
463 present (Figs. 2f, 7c, 8b), which was also likely generated from a chemical reaction with the
464 silicate melt. In contrast to our observations, lunar armalcolites exhibit an inverse core-rim
465 relationship of ilmenite and armalcolite with the latter forming the core (El Goresy et al. 1974;
466 Smyth 1974; Kesson and Lindsley 1975), which therefore indicates different possible modes of
467 formation.

468

469 **Formation of rutile within aggregates and magnetite outside aggregates**

470 From the 23 Fe-Ti-oxide aggregates analyzed from Zipplingen, 10 display magnetite rims on the
471 boundary towards the (devitrified) matrix and rutile within the aggregate core (Fig. 3, 7a-e,
472 Tab.1). The phase assemblage resembles a Fe concentration gradient, where the rim is enriched in
473 Fe, residing within µm-sized sub(-euhedral) magnetite (Fe_3O_4; Fig. 3a, g). Further inwards, the Fe
474 content decreases to ilmenite ($FeTiO_3$) and finally, Fe is absent, where rutile (TiO_2) exists (Figs.
475 3a, g, 7a-e). Moreover, the occurrence of ferropseudobrookite and/or rutile within the Fe-Ti-oxide

This is the peer-reviewed, final accepted version for American Mineralogist, published by the Mineralogical Society of America.
The published version is subject to change. Cite as Authors (Year) Title. American Mineralogist, in press.
DOI: https://doi.org/10.2138/am-2023-8985. http://www.minsocam.org/

aggregates (Figs. 7c-f, 8b, d) correlates with the presence of µm-sized (sub-)euhedral magnetite at the rim or in proximity to the (devitrified) glass. Only two ilmenite aggregates were observed without magnetite rims — they contain neither rutile nor ferropseudobrookite (Tab. 2).

We suggest that the association of µm-sized rutile along ilmenite grain boundaries included in the aggregates (Figs. 3c, d, 7c-e) was generated due to the thermal decomposition of ilmenite to rutile and Fe^0 after generation of the ilmenite aggregates, i.e., after shock unloading and under a low oxygen fugacity at temperatures ranging from 850° to 1050°C (Taylor et al. 1972) along sites of increased diffusivity like grain boundaries:

$$FeTiO_3 \rightarrow TiO_2 + Fe + \tfrac{1}{2}O_2 \quad \text{(Eq. 6)}$$

However, a sub-solidus re-equilibration, where ferropseudobrookite first formed at grain boundaries at the expense of ilmenite, with a subsequent back-transformation during cooling below 1140°C (Lindsley 1965) could, furthermore, lead to the formation of ilmenite and rutile (Haggerty and Lindsley 1969; Haggerty 1983; Anovitz et al. 1985):

$$FeTi_2O_5 \rightarrow FeTiO_3 + TiO_2 \quad \text{(Eq. 7)}$$

Experiments under temperatures from 900° to 1350°C with ilmenite and reducing agents of C (Gupta et al. 1990), CO (Zhao and Shadman 1990), or H_2 (Sargeant et al. 2020) generally form elemental iron at the rim, which is interpreted as a migration of iron towards the grain boundaries (Zhao and Shadman 1990; Kucukkaragoz and Eric 2006). Furthermore, ilmenite, rutile, and iron within the product aggregates can form through diffusion of a reducing agent into ilmenite along vacancies and/or pathways through interstitial structures, such as grain boundaries (Merk and Pickles 1988; Dang et al. 2015; Sargeant et al. 2020).

This is the peer-reviewed, final accepted version for American Mineralogist, published by the Mineralogical Society of America.
The published version is subject to change. Cite as Authors (Year) Title. American Mineralogist, in press.
DOI: https://doi.org/10.2138/am-2023-8985. http://www.minsocam.org/

497 The presence of a reducing agent could donate electrons to ilmenite at the rim, where Fe^{2+} is
498 reduced to Fe^0. More available electrons would then generate a gradient attracting Fe^{2+} to diffuse
499 from within the aggregate, which agrees with fast Fe^{2+} diffusion in ilmenite modelled by
500 Kuganathan et al. (2019). As a result, Fe^{2+} diffuses towards the rim and vacancies towards the
501 core, thereby leaving TiO_2 inside the ilmenite aggregates, as observed in our study (Figs. 3a, g,
502 6a). Consistently, we observe an increasing Fe/Ti ratio for ilmenite from the core of the
503 aggregates towards the rim (Fig. 3g, h; Tab. S1). Therefore, we interpret the process of iron
504 enrichment at the rims of the aggregates in terms of an electrochemical solid-state model, where
505 ilmenite aggregates serve as the anode and a reducing agent as the cathode, which generates an
506 electrochemical potential as a driving force for Fe^{2+} diffusion inside the ion-conducting ilmenite
507 (Kuganathan et al. 2019).

508 The high-temperature (>1140°C) phase transformation of ilmenite to ferropseudobrookite (Eq. 3)
509 only occurs at a low oxygen fugacity and results in the formation of FeO (Lindsley 1965), which
510 was not observed throughout the sample. We suggest that the absence of FeO together with the
511 pores within ferropseudobrookite (Fig. 7c-e) as well as magnetite along the rim (Fig. 7b, e) are
512 also the result of Fe^{2+} migration towards the Fe-Ti-oxide aggregate – melt/matrix boundary. In
513 general, the oxygen fugacity and thus the Fe^{3+}/Fe^{2+} ratio increases with decreasing temperature in
514 silicate melts (Sack et al. 1981; Kilinc et al. 1983). Therefore, oxidation of elemental iron along
515 the Fe-Ti-oxide boundaries could form magnetite at intermediate oxygen fugacity conditions, as
516 experimentally produced from 400° to 700°C (Mitchell et al. 1982; Kuroda and Mitchell 1983).
517 The experiments of Kuroda and Mitchell (1983) produced dispersed oriented magnetite as the
518 first iron oxide phase to form, as observed in our study:

519 $$3Fe + 2O_2 \rightarrow Fe_3O_4 \text{ (Eq. 8)}$$

The formation of armalcolite leads to a local enrichment of FeO in the silicate melt (Eqs. 4, 5), which likely contributed to the (sub-)euhedral magnetite due to oxidation, as observed within the matrix (Figs. 1a, 2e, 3e, 7a, f):

$$3FeO + ½O_2 \rightarrow Fe_3O_4 \text{ (Eq. 9)}$$

Magnetite formation by oxidation of ilmenite can be excluded because the reaction would stoichiometrically lead to the additional formation and local enrichment of TiO_2, which is not observed at the Fe-Ti-oxide boundaries:

$$3FeTiO_3 + ½O_2 \rightarrow Fe_3O_4 + 3TiO_2 \text{ (Eq. 10)}$$

Furthermore, oxidation of ilmenite above 800°C would only form pseudobrookite (Fe_2TiO_5) and hematite (Fe_2O_3) (Fu et al., 2010). Neither of the ferric phases were observed in the sample material from Zipplingen.

Fluorite-structured TiO_2 and rock salt-structured FeO were experimentally generated from ilmenite at shock pressures >60 GPa (Liu 1975; King and Ahrens 1976). In our study, TiO_2 is observed structurally only as rutile (Fig. 2b) and generally occurs within the cores of the Fe-Ti-oxide aggregates (Fig. 3a, g) or along grain boundaries of single ilmenite grains (Figs. 3c, d, 7c, d, e), and not together with a Fe-rich phase, as could be expected for the breakdown of ilmenite to FeO and TiO_2. We cannot exclude that other breakdown reactions of ilmenite took place in addition to the described breakdown reactions in the presence of a reducing agent but we do not observe evidence from the microfabric.

The investigated sample from Zipplingen consists of ≈15% of calcite, which either occurs as globules within the (devitrified) silicate matrix or as coarse xenomorphic calcite grains incorporating globules of (devitrified) silicate glass (Fig. 1b). The calcite phase boundary is

542 irregular and concave with respect to the silicate matrix. Philpotts and Ague (2009) used such
543 observations to interpret a silicate and an adjacent carbonatic melt based on the viscosities and,
544 therefore, the surface energies of the respective systems. Graup (1999) discussed a liquid
545 immiscibility of silicate and carbonatic melt in suevites from Zipplingen, which is in agreement
546 with Osinski et al. (2008), who considered melting as the common behavior of calcite in impact
547 cratering. On the other hand, Hörz et al. (2015, 2020) proposed devolatilization of calcite as the
548 dominant process based on SEM, electron microprobe analysis, thermal analyses, and shock
549 experiments. Temperatures of a melt vapor mixture formed from basement gneisses, where the
550 ilmenites from our study were likely derived, were modelled to be in excess of 2000°C (von
551 Engelhardt and Graup 1984). Carbonaceous sedimentary target rocks were first hit by the
552 impactor and thus experienced even higher temperature conditions (Bolten and Müller 1969).
553 Thermal decomposition of calcite produces CO_2 at temperatures above ≈650°C (Galwey and
554 Brown 1999) and CO when temperatures exceed 1500°C (Itoh et al. 1993). Furthermore, the
555 initial impact melt was presumably at pressure conditions above the stability conditions for CO_2.
556 Above 30 GPa, oxygen and diamond can form, which during subsequent unloading may react to
557 CO (Nellis et al. 1991; Tschauner et al. 2001). Overall, we suggest CO as a potential reducing
558 agent, which was mixed into the silicate melt due to suevite formation.

559 Ilmenites in lunar basaltic breccia have ≈3 μm spaced, parallel veins of rutile in combination with
560 droplets of metallic iron inside glass with a well-developed flow texture containing trains of
561 minute iron spherules (Sclar et al. 1973). Ilmenite aggregates were not reported to be enriched in
562 Fe at the ilmenite-glass phase boundary. The presence of a reducing agent as a result of the Ries
563 impact could, therefore, explain the iron-enriched rim of the Fe-Ti-oxide aggregates in
564 comparison to lunar samples, where elemental iron is occurring within the grain (Sclar et al.
565 1973).

566

567 **Pseudorutile formation**

568 In the Aumühle gneiss (R20-16A), pseudorutile ($Fe_2Ti_3O_9$) forms a rim around individual
569 ilmenite grains within the aggregates (Fig. 9c, d) or as a nearly complete replacement of coarse
570 ilmenite (Fig. 9e). Broad peaks in the Raman spectra indicate a fairly amorphous structure (Fig.
571 2h) (Imperial et al. 2022). Ilmenite alteration to pseudorutile occurs when water acts as a
572 transport medium for iron leaching (Mücke and Bhadra Chaudhuri 1991) at a high oxygen
573 fugacity below 700°C (Gupta et al. 1991), which proceeds along grain boundaries and structural
574 discontinuities within the grain (Teufer and Temple 1966; Temple 1966; Grey and Reid 1975).
575 Ilmenite aggregates in sample R20-16A have intergranular microcracks (Fig. 9b), which could
576 have allowed fluids to circulate along the grain boundaries, thereby favoring pseudorutile
577 formation surrounding single ilmenite grains during a late stage of hydrothermal activity. A
578 paleomagnetic study by Sleptsova et al. (2022) shows that the suevites from Aumühle, including
579 from sample R20-16A, were partially overprinted by hydrothermal activity, compatible with our
580 observations. Arp et al. (2013) suggested hydrothermal activity lasted ≈250 ka after the Ries
581 impact.

582

583 **Outlook and implications**

584 The interpretations of our study rely on experiments conducted in thermodynamic equilibrium.
585 The shock conditions during meteorite impacts, however, are far from thermodynamic
586 equilibrium conditions (Melosh 1989; Stöffler et al. 2018). Future shock experiments with
587 subsequent high-temperature quenching under controlled oxygen fugacity should yield insight

588 into more realistic temperature, pressure, and oxygen fugacity conditions of shocked ilmenites in
589 the natural environment.

590 Ilmenite-bearing material, such as the regolith of the moon, may constitute an in-situ oxygen
591 source (Badescu 2012 and references therein) and produces water when heated to temperatures
592 between 850° and 1050°C and reduced with H_2 (Li et al. 2012; Dang et al. 2015; Sargeant et al.
593 2020). Our study demonstrates that ilmenite microfabrics can be largely modified due to
594 meteorite impacts, resulting in aggregates that consist of various Fe- and/or Ti-bearing phases,
595 which change the physical, chemical, and/or magnetic properties of the host rocks. Our findings
596 might also be relevant for the consideration of breakdown reactions of Fe/Ti-phases in the scope
597 of in-situ resource utilization (ISRU) on planetary objects, whose surfaces are blanketed by
598 meteorite impact structures.

599

600 **Conclusions and summary**

601 The homogeneously distributed ilmenite aggregates within the investigated samples contain a
602 suite of Fe-Ti-oxide phases created by pressure-, temperature-, and oxygen-fugacity-changes
603 during impact cratering. Figure 11 summarizes our proposed scenario of how the modification of
604 ilmenite via solid-state transformation through time can explain the phase assemblages in the Ries
605 impact structure.

606 (I) Upon shock loading, target ilmenites were (partly) transformed into the high-pressure phase
607 liuite (>16 GPa), then transformed upon unloading to wangdaodeite and subsequently ilmenite
608 forming a foam structure (Fig. 11-I). In ≈5% of the observed cases, shocked ilmenite is preserved
609 in the core of the aggregates, which can contain transformation twins that share a common

610 $\{11\bar{2}0\}$ plane with the host and the *c-axis* is oriented at an angle of 109° to that of the host (Figs.
611 4, 5a, 6b). The transformation from the high-pressure phase liuite is reflected by the
612 crystallographic relationship of the new grains that exhibit up to three orientation domains that
613 share a common $\{11\bar{2}0\}$ plane and whose *c*-axes enclose angles of 109° and 99°, respectively,
614 similar to the twin lamellae within the only partly transformed remnant shocked ilmenite (Fig. 5),
615 which are suggested to represent transformational twins (Fig. 10).

616 (II+III+IV) Heat production during shock unloading leads to a decrease in oxygen fugacity,
617 however, high-temperature gradients produce different phases and microfabrics. The formation of
618 ferropseudobrookite from ilmenite, occurring mostly at aggregate boundaries and along fractures
619 (Fig. 11-II), indicates temperatures >1140°C with a low oxygen fugacity. Rutile grains along
620 boundaries of ilmenite in the aggregates (Fig. 11-III) indicate thermal decomposition of ilmenite
621 between 850° and 1050°C favored along sites of increased diffusivity. The presence of a reducing
622 agent (likely CO) generated an electron enrichment, which resulted in an electrochemical
623 potential driving Fe^{2+} to migrate from within the ilmenite aggregate cores towards the rim,
624 forming TiO_2 inside the ilmenite aggregates (Fig. 11-IV). Depending on whether the influence of
625 heating or reduction locally prevailed, either μm-sized rutile on grain boundaries (Fig. 11-III) or
626 larger TiO_2 residues were formed (Fig. 11-IV), respectively. The chemical interaction of the
627 silicate melt with ferropseudobrookite formed rare armalcolite-ferropseudobrookite solid solution
628 (Fig. 8a, b, h).

629 (V) Oxygen fugacity increased as temperature decreased after the impact, which oxidized the
630 iron-enriched rim of the ilmenite aggregates, thereby resulting in the formation of μm-sized (sub-
631)euhedral magnetite (Fig. 11-V).

(VI) In the aftermath of the impact at temperatures <700°C in combination with high oxygen fugacity, pseudorutile locally formed along intergranular cracks within the ilmenite aggregate in the presence of a fluid (Fig. 11-VI).

Acknowledgements

We greatly appreciate the constructive and thoughtful comments of Aaron Cavosie and an anonymous reviewer as well as the editorial handling of Susannah Dorfman. We thank Dirk Müller for the help with the electron microprobe analyses, Jean Pohl for his helpful comments on the manuscript, and Rhander Taufner for help with the MTEX scripts. We acknowledge financial support from the Deutsche Forschungsgemeinschaft TR534/9-1 and GI712/20-1.

References

Abrahams, S.C., Reddy, J.M., and Bernstein, J.L. (1966) Ferroelectric lithium niobate. 3. Single crystal X-ray diffraction study at 24°C. Journal of Physics and Chemistry of Solids, 27, 997–1012.

Anderson, A.T., Boyd, F.R., Bunch, T.E., Cameron, E.N., El Goresy, A., and Finger, L.W. (1970) Armalcolite: A new mineral from the Apollo 11 samples. In Geochimica et Cosmochimica Acta Supplement Vol. 1, p. 55.

Anovitz, L.M., Treiman, A.H., Essene, E.J., Hemingway, B.S., Westrum, E.F., Wall, V.J., Burriel, R., and Bohlen, S.R. (1985) The heat-capacity of ilmenite and phase equilibria in the system Fe-T-O. Geochimica et Cosmochimica Acta, 49, 2027–2040.

Arp, G., Kolepka, C., Simon, K., Karius, V., Nolte, N., and Hansen, B.T. (2013) New evidence for persistent impact-generated hydrothermal activity in the Miocene Ries impact structure, Germany. Meteoritics and Planetary Science, 48, 2491–2516.

Badescu, V., Ed. (2012) Moon. Springer Berlin Heidelberg, Berlin, Heidelberg.

Barth, T.F.W., and Posnjak, E. (1934) The Crystal Structure of Ilmenite. Zeitschrift für Kristallographie - Crystalline Materials, 88, 265–270.

Bauer, M., Davydovskaya, P., Janko, M., Kaliwoda, M., Petersen, N., Gilder, S.A., and Stark, R.W. (2011) Raman spectroscopy of laser-induced oxidation of titanomagnetites. Journal of Raman Spectroscopy, 42, 1413–1418.

Bolten, R., and Müller, D. (1969) Das Tertiär im Nördlinger Ries und in seiner Umgebung. Geologica Bavarica, 61, 87–130.

Bowles, J.F.W. (1988) Definition and range of composition of naturally occurring minerals with the pseudobrookite structure. American Mineralogist, 73, 1377–1383.

Bueble, S., Knorr, K., Brecht, E., and Schmahl, W.W. (1998) Influence of the ferroelastic twin domain structure on the {100} surface morphology of $LaAlO_3$ HTSC substrates. Surface Science, 400, 345–355.

Cavosie, A.J., Timms, N.E., Ferrière, L., and Rochette, P. (2018) FRIGN zircon-The only terrestrial mineral diagnostic of high-pressure and high-temperature shock deformation. Geology, 46, 891–894.

Cynn, H., Sharma, S.K., Cooney, T.F., and Nicol, M. (1992) High-temperature Raman investigation of order-disorder behavior in the $MgAl_2O_4$ spinel. Physical Review B, 45, 500–502.

674 Dang, J., Zhang, G.H., and Chou, K.C. (2015) Kinetics and mechanism of hydrogen reduction of
675 ilmenite powders. Journal of Alloys and Compounds, 619, 443–451.

676 Dellefant, F., Trepmann, C.A., Gilder, S.A., Sleptsova, I. V, Kaliwoda, M., and Weiss, B.P.
677 (2022) Ilmenite and magnetite microfabrics in shocked gneisses from the Vredefort impact
678 structure, South Africa. Contributions to Mineralogy and Petrology, 5.

679 Di Vincenzo, G. (2022) High precision multi-collector $^{40}Ar/^{39}Ar$ dating of moldavites (Central
680 European tektites) reconciles geochrological and paleomagnetic data. Chemical Geology,
681 608, 121026.

682 Drury, M.R., and Urai, J.L. (1990) Deformation-related recrystallization processes.
683 Tectonophysics, 172, 235–253.

684 El Goresy, A. (1964) Die Erzmineralien in den Ries- und Bosumtwi-Krater-Gläsern und ihre
685 genetische deutung. Geochimica et Cosmochimica Acta, 28.

686 El Goresy, A., and Chao, E.C.T. (1976) Identification and significance of armalcolite in the Ries
687 glass. Earth and Planetary Science Letters, 30, 200–208.

688 El Goresy, A., Ramdohr, P., Medenbach, O., and Bernhardt, H.-J. (1974) Taurus-Littrow TiO_2-
689 basalts: Opaque mineralogy and geochemistry. In Geochimica et Cosmochimica Acta
690 Supplement Vol. 1, pp. 627–652.

691 El Goresy, A., Dubrovinsky, L., Gillet, P., Graup, G., and Chen, M. (2010) Akaogiite: An ultra-
692 dense polymorph of TiO_2 with the baddeleyite-type structure, in shocked garnet gneiss from
693 the Ries Crater, Germany. American Mineralogist, 95, 892–895.

694 Erickson, T.M., Pearce, M.A., Reddy, S.M., Timms, N.E., Cavosie, A.J., Bourdet, J., Rickard,
695 W.D.A., and Nemchin, A.A. (2017) Microstructural constraints on the mechanisms of the

transformation to reidite in naturally shocked zircon. Contributions to Mineralogy and Petrology, 172.

Eriksson, G., and Pelton, A.D. (1993) Critical evaluation and optimization of the thermodynamic properties and phase diagrams of the CaO-Al_2O_3, Al_2O_3-SiO_2, and CaO-Al_2O_3-SiO_2 systems. Metallurgical Transactions B, 24, 807–816.

Evans, B., Renner, J., and Hirth, G. (2001) A few remarks on the kinetics of static grain growth in rocks. International Journal of Earth Sciences, 90, 88–103.

Frick, C. (1973) Kimberlitic Ilmenites. South African Journal of Geology, 76, 85–94.

Fu, X., Wang, Y., and Wei, F. (2010) Phase transitions and reaction mechanism of ilmenite oxidation. Metallurgical and Materials Transactions A: Physical Metallurgy and Materials Science, 41, 1338–1348.

Fujimaki, H., Matsu-Ura, M., Sunagawa, I., and Aoki, K. (1981) Chemical compositions of chondrules and matrices in the ALH-77015 chondrite (L3). Memoirs of National Institute of Polar Research. Special issue, 20, 161–174.

Galwey, A.K., and Brown, M.E. (1999) Thermal Decomposition of Ionic Solids, 596 p. Vol. 86. Elsevier.

Graup, G. (1999) Carbonate-silicate liquid immiscibility upon impact melting: Ries Crater, Germany. Meteoritics and Planetary Science, 34, 425–438.

Grégoire, M., Lorand, J.P., O'Reilly, S.Y., and Cottin, J.Y. (2000) Armalcolite-bearing, Ti-rich metasomatic assemblages in harzburgitic xenoliths from the Kerguelen Islands: Implications for the oceanic mantle budget of high-field strength elements. Geochimica et Cosmochimica Acta, 64, 673–694.

718 Grey, I.E., and Reid, A.F. (1975) The Structure of Pseudorutile and Its Role in The Natural
719 Alteration of llmenite. The American Mineralogist, 60, 898–906.

720 Gupta, S.K., Rajakumar, V., and Grieveson, P. (1990) The role of preheating in the kinetics of
721 reduction of ilmenite with carbon. Canadian Metallurgical Quarterly, 29, 43–49.

722 Gupta, S.K., Rajakumar, V., and Grieveson, P. (1991) Phase transformations during heating of
723 llmenite concentrates. Metallurgical Transactions B, 22, 711–716.

724 Haggerty, S.E. (1973) Armalcolite and genetically associated opaque minerals in the lunar
725 samples. In Proceedings of the Fourth Lunar Science Conference Vol. 1, pp. 777–797.

726 Haggerty, S.E. (1975) The chemistry and genesis of opaque minerals in kimberlites. Physics and
727 Chemistry of the Earth, 9, 295–307.

728 Haggerty, S.E. (1983) The mineral chemistry of new titanates from the jagersfontein kimberlite,
729 South Africa: Implications for metasomatism in the upper mantle. Geochimica et
730 Cosmochimica Acta, 47, 1833–1854.

731 ——— (1991) Oxide Textures - A Mini-Atlas. Reviews in Mineralogyv, 25, 129–219.

732 Haggerty, S.E., and Lindsley, D.H. (1969) Stabihty of the pseudobrookite (Fe_2TiO_5)-
733 ferropseudobrookite ($FeTi_2O_5$) series. In Carniege Institution of Washington Yearbook 68
734 pp. 247–249.

735 Hahn, T., and Klapper, H. (2006) Twinning of crystals. In International Tables for
736 Crystallography Vol. D, pp. 393–448. International Union of Crystallography, Chester,
737 England.

738 Hashishin, T., Tan, Z., Yamamoto, K., Qiu, N., Kim, J., Numako, C., Naka, T., Valmalette, J.C.,

and Ohara, S. (2014) Quenching ilmenite with a high-temperature and high-pressure phase using super-high-energy ball milling. Scientific Reports, 4, 1–6.

Hayob, J.L., and Essene, E.J. (1995) Armalcolite in crustal paragneiss xenoliths, central Mexico. American Mineralogist, 80, 810–822.

He, M., Winkler, B., Bauer, J.D., Bayarjargal, L., Ruiz-Fuertes, J., Alencar, I., Morgenroth, W., Refson, K., and Milman, V. (2017) Lattice dynamics and Mg/Ti order in orthorhombic pseudobrookite-type $MgTi_2O_5$. Journal of Alloys and Compounds, 699, 16–24.

Hörz, F., Archer, P.D., Niles, P.B., Zolensky, M.E., and Evans, M. (2015) Devolatilization or melting of carbonates at Meteor Crater, AZ? Meteoritics and Planetary Science, 50, 1050–1070.

Hörz, F., Cintala, M.J., Thomas-Keprta, K.L., Ross, D.K., and Clemett, S.J. (2020) Unconfined shock experiments: A pilot study into the shock-induced melting and devolatilization of calcite. Meteoritics and Planetary Science, 55, 102–129.

Hüttner, R., and Schmidt-Kaler, H. (1999) Die Geologische Karte des Rieses 1: 50 000 (2., überarbeitete Auflage). Geologica Bavarica, 104, 7–76.

Imperial, A., Pe-Piper, G., Piper, D.J.W., and Grey, I.E. (2022) Identifying Pseudorutile and Kleberite Using Raman Spectroscopy. Minerals, 12, 1210.

Itoh, N., Sanchez, M.A., Xu, W.C., Haraya, K., and Hongo, M. (1993) Application of a membrane reactor system to thermal decomposition of CO_2. Journal of Membrane Science, 77, 245–253.

Janovec, V., and Přívratská, J. (2006) Domain structures. In International Tables for Crystallography Vol. D, pp. 449–505. International Union of Crystallography, Chester,

761 England.

762 Kaliwoda, M., Giordano, D., Krüger, M.E., Uysal, I., Akmaz, M.R., Hoffmann, V., Hochleitner,
763 R., and Schmahl, W.W. (2021) Raman spectroscopy as a tool for the quantitative estimate of
764 chromium aluminium oxide content in chromite. Spectroscopy, 36, 17–23.

765 Keil, K., Prinz, M., and Bunch, T.E. (1970) Mineral Chemistry of Lunar Samples. Science, 167,
766 597–599.

767 Kesson, S.E., and Lindsley, D.H. (1975) The effects of Al^{3+}, Cr^{3+}, and Ti^{3+} on the stability of
768 armalcolite. Proceedings of the 6th Lunar Science Conference, 911–920.

769 Kilinc, A., Carmichael, I.S.E., Rivers, M.L., and Sack, R.O. (1983) The ferric-ferrous ratio of
770 natural silicate liquids equilibrated in air. Contributions to Mineralogy and Petrology, 83,
771 136–140.

772 King, D.A., and Ahrens, T.J. (1976) Shock compression of ilmenite. Journal of Geophysical
773 Research, 81, 931–935.

774 Kostrovitsky, S.I., Yakovlev, D.A., Soltys, A., Ivanov, A.S., Matsyuk, S.S., and Robles-Cruz,
775 S.E. (2020) A genetic relationship between magnesian ilmenite and kimberlites of the
776 Yakutian diamond fields. Ore Geology Reviews, 120, 103419.

777 Kucukkaragoz, C.S., and Eric, R.H. (2006) Solid state reduction of a natural ilmenite. Minerals
778 Engineering, 19, 334–337.

779 Kuganathan, N., Srikaran, R., Fossati, P.C.M., and Chroneos, A. (2019) Theoretical Modeling of
780 Defects, Dopants, and Diffusion in the Mineral Ilmenite. Minerals, 9, 610.

781 Kuroda, K., and Mitchell, T.E. (1983) TEM studies of oxidation and passivation of iron. In R.M.

782 Fisher, R. Gronsly, and K.H. Wetmacott, Eds., Seventh International Conference on High
783 Voltage Electron Microscopy pp. 261–267. University of California, Berkeley.

784 Leinenweber, K., Utsumi, W., Tsuchida, Y., Yagi, T., and Kurita, K. (1991) Unquenchable high-
785 pressure perovskite polymorphs of $MnSnO_3$ and $FeTiO_3$. Physics and Chemistry of
786 Minerals, 18, 244–250.

787 Leinenweber, K., Yanbin Wang, Yagi, T., and Yusa, H. (1994) An unquenchable perovskite
788 phase of $MgGeO_3$ and comparison with $MgSiO_3$ perovskite. American Mineralogist, 79,
789 197–199.

790 Li, Y., Li, X., Wang, S., Tang, H., Gan, H., Li, S., and Ouyang, Z. (2012) In-situ water
791 production by reducing ilmenite. In V. Badescu, Ed., Moon pp. 189–200. Springer, New
792 York.

793 Liermann, H.P., Downs, R.T., and Yang, H. (2006) Site disorder revealed through Raman spectra
794 from oriented single crystals: A case study on karooite ($MgTi_2O_5$). American Mineralogist,
795 91, 790–793.

796 Lindsley, D.H. (1965) Iron-Titanium Oxides. In Carniege Institute Washington Yearbook 64 pp.
797 144–148.

798 Lindsley, D.H., Kesson, S.E., Hartzman, M.J., and Cushman, M.K. (1974) The stability of
799 armacolite: Experimantal studies in the system MgO-Fe-Ti-O. In Proceedings of the Fifth
800 Lunar Conference pp. 521–534. Pergamon Press.

801 Liu, L.G. (1975) High-pressure phase transformations and compressions of ilmenite and rutile, I.
802 Experimental results. Physics of the Earth and Planetary Interiors, 10, 167–176.

803 Ma, C., and Tschauner, O. (2018) Liuite, IMA 2017-042a. CNMNC Newsletter No. 46.

804 Mineralogical Magazine, 82, 1369–1379.

805 Mazza, T., Barborini, E., Piseri, P., Milani, P., Cattaneo, D., Li Bassi, A., Bottani, C.E., and
806 Ducati, C. (2007) Raman spectroscopy characterization of TiO_2 rutile nanocrystals. Physical
807 Review B - Condensed Matter and Materials Physics, 75, 1–5.

808 Mehta, A., Leinenweber, K., Navrotsky, A., and Akaogi, M. (1994) Calorimetric study of high
809 pressure polymorphism in $FeTiO_3$: Stability of the perovskite phase. Physics and Chemistry
810 of Minerals, 21, 207–212.

811 Melosh, H.J. (1989) Impact cratering: a geologic process, 245 p. Oxford University Press, New
812 York.

813 Merk, R., and Pickles, C.A. (1988) Reduction of ilmenite by carbon monoxide. Canadian
814 Metallurgical Quarterly, 27, 1–7.

815 Ming, L.C., Kim, Y.H., Uchida, T., Wang, Y., and Rivers, M. (2006) In situ X-ray diffraction
816 study of phase transitions of $FeTiO_3$ at high pressures and temperatures using a large-volume
817 press and synchrotron radiation. American Mineralogist, 91, 120–126.

818 Minkin, J.A., and Chao, E.C.T. (1971) Single crystal X-ray investigation of deformation in
819 terrestrial and lunar ilmenite. In Proceedings of the Second Lunar Science Conference pp.
820 237–246. M.I.T. Press.

821 Mitchell, R.H. (1973) Magnesian Ilmenite and Its Role in Kimberlite Petrogenesis. The Journal
822 of Geology, 81, 301–311.

823 Mitchell, T.E., Voss, D.A., and Butler, E.P. (1982) The observation of stress effects during the
824 high temperature oxidation of iron. Journal of Materials Science, 17, 1825–1833.

825 Mücke, A., and Bhadra Chaudhuri, J.N. (1991) The continuous alteration of ilmenite through
826 pseudorutile to leucoxene. Ore Geology Reviews, 6, 25–44.

827 Nellis, W.J., Mitchell, A.C., Ree, F.H., Ross, M., Holmes, N.C., Trainor, R.J., and Erskine, D.J.
828 (1991) Equation of state of shock-compressed liquids: Carbon dioxide and air. The Journal
829 of Chemical Physics, 95, 5268–5272.

830 Nicolas, A., and Poirier, J.P., 1976. Crystalline Plasticity and Solid State Flow in Metamorphic
831 Rocks. John Wiley & Sons, New York.

832 Nishio-Hamane, D., Yagi, T., Ohshiro, M., Niwa, K., Okada, T., and Seto, Y. (2010)
833 Decomposition of perovskite $FeTiO_3$ into wüstite $Fe_{1-x}Ti_{0.5x}O$ and orthorhombic $FeTi_3O_7$ at
834 high pressure. Physical Review B, 82, 092103.

835 Nishio-Hamane, D., Zhang, M., Yagi, T., and Ma, Y. (2012) High-pressure and high-temperature
836 phase transitions in $FeTiO_3$ and a new dense $FeTi_3O_7$ structure. American Mineralogist, 97,
837 568–572.

838 Osinski, G.R., Spray, J.G., and Grieve, R.A.F. (2008) Impact melting in sedimentary target rocks:
839 An assessment. Special Paper of the Geological Society of America, 437, 1–18.

840 Pantić, J., Urbanovich, V., Poharc-Logar, V., Jokić, B., Stojmenović, M., Kremenović, A., and
841 Matović, B. (2014) Synthesis and characterization of high-pressure and high-temperature
842 sphene ($CaTiSiO_5$). Physics and Chemistry of Minerals, 41, 775–782.

843 Pasteris, J.D. (1980) The significance of groundmass ilmenite and megacryst ilmenite in
844 kimberlites. Contributions to Mineralogy and Petrology, 75, 315–325.

845 Philpotts, A., and Ague, J. (2009) Principles of Igneous and Metamorphic Petrology, 2nd ed., 667
846 p. Cambridge University Press, New York.

847 Pilkington, M., and Grieve, R.A.F. (1992) The geophysical signature of terrestrial impact craters.
848 Reviews of Geophysics, 30, 161–181.

849 Pilkington, M., and Hildebrand, A.R. (2000) Three-dimensional magnetic imaging of the
850 Chicxulub Crater. Journal of Geophysical Research: Solid Earth, 105, 23479–23491.

851 Plado, J., Pesonen, L.J., and Puura, V. (1999) Effect of erosion on gravity and magnetic
852 signatures of complex impact structures: Geophysical modeling and applications. In B.O.
853 Dressler and V.L. Sharpton, Eds., Special Paper of the Geological Society of America Vol.
854 339, pp. 229–239. Geological Society of America, Boulder, Colorado.

855 Pohl, J., Stöffler, D., Gall, H., and Ernston, K. (1977) The Ries impact crater. In D.J. Roddy, R.O.
856 Pepin, and R.B. Merrill, Eds., Impact and Explosion Cratering pp. 343–404. Pergamon
857 Press, New York.

858 Pohl, J., Poschlod, K., Reimold, W.U., Meyer, C., and Jacob, J. (2010) Ries crater, Germany: The
859 Enkingen magnetic anomaly and associated drill core SUBO 18. In R.L. Gibson and W.U.
860 Reimold, Eds., Large Meteorite Impacts and Planetary Evolution IV Vol. 465, pp. 141–163.
861 Geological Society of America.

862 Rocholl, A., Schaltegger, U., Gilg, H.A., Wijbrans, J., and Böhme, M. (2017) The age of volcanic
863 tuffs from the Upper Freshwater Molasse (North Alpine Foreland Basin) and their possible
864 use for tephrostratigraphic correlations across Europe for the Middle Miocene. International
865 Journal of Earth Sciences, 107, 387–407.

866 Rocholl, A., Böhme, M., Gilg, H.A., Pohl, J., Schaltegger, U., and Wijbrans, J. (2018) Comment
867 on "A high-precision $^{40}Ar/^{39}Ar$ age for the Nördlinger Ries impact crater, Germany, and
868 implications for the accurate dating of terrestrial impact events" by Schmieder et al.

(Geochimica et Cosmochimica Acta 220 (2018) 146–157). Geochimica et Cosmochimica Acta, 238, 599–601.

Sack, R.O., Carmichael, I.S.E., Rivers, M., and Ghiorso, M.S. (1981) Ferric-ferrous equilibria in natural silicate liquids at 1 bar. Contributions to Mineralogy and Petrology, 75, 369–376.

Sargeant, H.M., Abernethy, F.A.J., Barber, S.J., Wright, I.P., Anand, M., Sheridan, S., and Morse, A. (2020) Hydrogen reduction of ilmenite: Towards an in situ resource utilization demonstration on the surface of the Moon. Planetary and Space Science, 180, 104751.

Schmidt-Kaler, H. (1969) Versuch einer Profildarstellung für das Rieszentrum vor der Kraterbildung. Geologica Bavarica, 61, 38–40.

Schmieder, M., Kennedy, T., Jourdan, F., Buchner, E., and Reimold, W.U. (2018a) A high-precision $^{40}Ar/^{39}Ar$ age for the Nördlinger Ries impact crater, Germany, and implications for the accurate dating of terrestrial impact events. Geochimica et Cosmochimica Acta, 220, 146–157.

——— (2018b) Response to comment on "A high-precision $^{40}Ar/^{39}Ar$ age for the Nördlinger Ries impact crater, Germany, and implications for the accurate dating of terrestrial impact events" by Schmieder et al. (Geochimica et Cosmochimica Acta 220 (2018) 146–157). Geochimica et Cosmochimica Acta, 238, 602–605.

Schwarz, W.H., Hanel, M., and Trieloff, M. (2020) U-Pb dating of zircons from an impact melt of the Nördlinger Ries crater. Meteoritics and Planetary Science, 55, 312–325.

Sclar, C.B., Bauer, J.F., Pickart, S.J., and Alperin, H.A. (1973) Shock effects in experimentally shocked terrestrial ilmenite, lunar ilmenite of rock fragments in 1-10 mm fines (10085,19), and lunar rock 60015,127. In Proceedings of the Fourth Lunar Science Conference Vol. 1,

pp. 841–859. Pergamon Press, Texas.

Scott, R.G., Pilkington, M., and Tanczyk, E.I. (1997) Magnetic investigations of the West Hawk, Deep Bay and Clearwater impact structures, Canada. Meteoritics and Planetary Science, 32, 293–308.

Sleptsova, I. V., Gilder, S.A., Dellefant, F., Trepmann, C.A., and Pohl, J. (2022) Remanent magnetization in Bunte Breccia from the Ries impact structure, Germany. In S. Frančišković-Bilinski, H. Böhnel, R. Egli, A. Hirt, E. Petrovský, S. Spassov, and T. Werner, Eds., 17th Castle Meeting p. 126.

Smyth, J.R. (1974) The crystal chemistry of armalcolites from Apollo 17. Earth and Planetary Science Letters, 24, 262–270.

Spiridonov, E.M., Semikolennykh, E.S., Lysenko, V.I., Filimonov, S. V., Korotayeva, N.N., and Krivitskaya, N.N. (2019) Armalcolite-Bearing Island Arc Plagiolherzolites and Olivine Gabbro–Norite–Dolerites of the Balaklava Area (Crimea). Moscow University Geology Bulletin, 74, 380–392.

Stöffler, D., and Grieve, R.A.F. (2007) Impactites. In D. Fettes and J. Desmons, Eds., Metamorphic Rocks: A Classification and Glossary of Terms, Recommendations of the International Union of Geological Sciences pp. 82–92, 111–125 and 126–242. Cambridge University Press, Cambridge.

Stöffler, D., Artemieva, N.A., Wünnemann, K., Reimold, W.U., Jacob, J., Hansen, B.K., and Summerson, I.A.T. (2013) Ries crater and suevite revisited-Observations and modeling Part I: Observations. Meteoritics & Planetary Science, 48, 515–589.

Stöffler, D., Hamann, C., and Metzler, K. (2018) Shock metamorphism of planetary silicate rocks

913 and sediments: Proposal for an updated classification system. Meteoritics & Planetary
914 Science, 53, 5–49.

915 Syono, Y., Takei, H., Goto, T., and Ito, A. (1981) Single crystal X-ray and Mössbauer study of
916 shocked ilmenite to 80 GPa. Physics and Chemistry of Minerals, 7, 82–87.

917 Taylor, L.A., Williams, R.J., and McCallister, R.H. (1972) Stability relations of ilmenite and
918 ulvöspinel in the Fe-Ti-O system and application of these data to lunar mineral assemblages.
919 Earth and Planetary Science Letters, 16, 282–288.

920 Temple, A.K. (1966) Alteration of ilmenite. Economic Geology, 61, 695–714.

921 Teufer, G., and Temple, A.K. (1966) Pseudorutile—a New Mineral Intermediate between
922 Ilmenite and Rutile in the N Alteration of Ilmenite. Nature, 211, 179–181.

923 Timms, N.E., Erickson, T.M., Pearce, M.A., Cavosie, A.J., Schmieder, M., Tohver, E., Reddy,
924 S.M., Zanetti, M.R., Nemchin, A.A., and Wittmann, A. (2017) A pressure-temperature phase
925 diagram for zircon at extreme conditions. Earth-Science Reviews, 165, 185–202.

926 Tschauner, O., Mao, H.K., and Hemley, R.J. (2001) New transformations of CO_2 at high
927 pressures and temperatures. Physical Review Letters, 87, 75701-1-75701–4.

928 Tschauner, O., Ma, C., Newville, M.G., and Lanzirotti, A. (2020) Structure analysis of natural
929 wangdaodeite—$LiNbO_3$-type $FeTiO_3$. Minerals, 10, 1–12.

930 Tuthill, R.L., and Sato, M. (1970) Phase relations of a simulated lunar basalt as a function of
931 oxygen fugacity, and their bearing on the petrogenesis of the Apollo 11 basalts. Geochimica
932 et Cosmochimica Acta, 34, 1293–1302.

933 Ugalde, H.A., Artemieva, N.A., and Milkereit, B. (2005) Magnetization on impact structures -

Constraints from numerical modeling and petrophysics. In T. Kenkmann, F. Hörz, and A. Deutsch, Eds., Large meteorite impacts III: Geological Society of America Special Paper 384 Vol. Special Pa, pp. 25–42. Geological Society of America, Boulder.

von Engelhardt, W., and Graup, G. (1984) Suevite of the Ries crater, Germany: Source rocks and implications for cratering mechanics. Geologische Rundschau, 73, 447–481.

von Engelhardt, W., Arndt, J., Fecker, B., and Pankau, H.G. (1995) Suevite breccia from the Ries crater, Germany: Origin, cooling history and devitrification of impact glasses. Meteoritics, 30, 279–293.

Wang, A., Kuebler, K.E., Jolliff, B.L., and Haskin, L.A. (2004) Raman spectroscopy of Fe-Ti-Cr-oxides, case study: Martian meteorite EETA79001. American Mineralogist, 89, 665–680.

Wang, Y., Liu, X., Yao, G.D., Liebermann, R.C., and Dudley, M. (1991) High temperature transmission electron microscopy and X-ray diffraction studies of twinning and the phase transition at 145°C in LaGaO3. Materials Science and Engineering A, 132, 13–21.

Weis, R.S., and Gaylord, T.K. (1985) Lithium niobate: Summary of physical properties and crystal structure. Applied Physics A Solids and Surfaces, 37, 191–203.

Wheeler, J., Prior, D.J., Jiang, Z., Spiess, R., and Trimby, P.W. (2001) The petrological significance of misorientations between grains. Contributions to Mineralogy and Petrology, 141, 109–124.

Wilson, N.C., Muscat, J., Mkhonto, D., Ngoepe, P.E., and Harrison, N.M. (2005) Structure and properties of ilmenite from first principles. Physical Review B - Condensed Matter and Materials Physics, 71, 1–9.

Wu X, Steinle-Neumann G, Narygina O, et al (2009) High-pressure behavior of perovskite:

$FeTiO_3$ dissociation into $(Fe_{1-\delta},Ti_\delta)O$ and $Fe_{1+\delta}Ti_{2-\delta}O_5$. Phys Rev Lett 103:1–4. https://doi.org/10.1103/PhysRevLett.103.065503

Wünnemann, K., Morgan, J. V., and Jödicke, H. (2005) Is ries crater typical for its size? An analysis based upon old and new geophysical data and numerical modeling. In T. Kenkmann, F. Hörz, and A. Deutsch, Eds., Large meteorite impacts III: Geological Society of America Special Paper 384 Vol. 384, pp. 67–83. Geological Society of America, Boulder.

Xie, X., Gu, X., Yang, H., Chen, M., and Li, K. (2020) Wangdaodeite, the $LiNbO_3$-structured high-pressure polymorph of ilmenite, a new mineral from the Suizhou L6 chondrite. Meteoritics and Planetary Science, 55, 184–192.

Zhao, Y., and Shadman, F. (1990) Kinetics and mechanism of ilmenite reduction with carbon monoxide. AIChE Journal, 36, 1433–1438.

Fig. 1 Polarized light micrographs of ilmenite- and other Fe-Ti-oxide aggregates within samples from the Ries impact structure. **a, b)** Glass fragment (Flädle; sample CT827a) from Zipplingen. **a)** Fe-Ti-oxide (fto) aggregates are associated with magnetite (Mag); reflected light. **b)** Homogeneously distributed Fe-Ti-oxide aggregates (white arrows) and calcite (Cal) within the matrix in reflected polarized light. Note the (devitrified) glass globules within calcite (Cal, yellow arrows) and calcite globules within the matrix (gl, orange arrows). The inset displays the irregular glass-calcite boundary in transmitted light with crossed polarizers. Note that calcite is concave with respect to the glass matrix. **c, d)** Strongly shocked gneiss clast (sample R20-16A) in suevite from the Aumühle quarry that contains ilmenite (Ilm) aggregates, secondary hematite (Hem), and

977 vesicles (vs) within a cryptocrystalline matrix (cr); (c) single plane-polarized reflected light, (d)
978 transmitted light and crossed polarizers.

979

980 **Fig. 2** Raman spectra of **(a)** ilmenite, **(b)** rutile, **(c)** ferropseudobrookite, **(d)** magnetite rim
981 surrounding ilmenite, **(e)** magnetite within the (devitrified) glass matrix, and **(f)** sphene within
982 sample CT827a; as well as **(g)** ilmenite and **(h)** pseudorutile within sample R20-16A.

983

984 **Fig. 3** SEM analyses of Fe-Ti-oxide aggregates embedded in a (devitrified) glass matrix (gl)
985 sample CT827a, Zipplingen; (a-e, g) are BSE images and (f) is a SE image. **a, b)** Foam-structured
986 ilmenite (Ilm) aggregate containing rutile (Rt; black) with a magnetite (Mag; white) rim. The
987 yellow rectangle displays the area depicted in (b). **c, d)** Foam-structured ilmenite (Ilm) aggregate
988 with isolated small rutile (Rt; black) grains along ilmenite boundaries. Note that the image
989 contrast was optimized to show the orientation contrast of ilmenite grains (grey shades), rutile
990 appears black. Magnetite (Mag; white) occurs at the rim. The yellow rectangle displays the area
991 depicted in (d). **e, f)** (Sub-)euhedral magnetite (Mag) occurring at the rim of Fe-Ti-oxide
992 aggregates. The yellow rectangle displays the area depicted in (f). **g)** Fe (green) and Ti (purple)
993 map of the aggregate consisting of ilmenite (Ilm) with rutile (Rt) in the core and a rim of
994 magnetite (Mag). The yellow arrow indicating the Fe/Ti gradient displayed in (h). **h)** Increasing
995 Fe/Ti gradient from the core towards the rim of the aggregate based on EMP data (Tab. S1).

996

997 **Fig. 4** EBSD data of ilmenite aggregate, sample CT827a, Zipplingen. **a)** Phase map of ilmenite
998 (red), magnetite (blue), and rutile (yellow). **b)** Orientation map (all Euler coloring) of (a). **c)**

Grain Reference Orientation Distribution map (GROD) displaying the angular deviation from the average grain orientation. Note the short wavelength misorientation pattern in the core. **d, e)** Pole figures of the {0001}, {11$\bar{2}$0}, and {10$\bar{1}$1} planes of the (d) coarse grain in the core and (e) polycrystalline ilmenite rim.

Fig. 5 Crystallographic orientations within ilmenite aggregates, sample CT827a, Zipplingen. **a)** Orientation map (inverse pole figure of z-direction) of rim and core, which displays twin lamellae (orange; twin boundaries in white). The blue and yellow triangles depict the positions of representative core and lamellae orientations depicted in (e). **b)** Orientation map (inverse pole figure of z-direction) with green, blue, and pink triangles, which depict the positions of representative crystallographic orientations displayed in (f). **c, d)** Pole figures and density plots of the {0001}, {11$\bar{2}$0}, and {10$\bar{1}$1}, corresponding to the orientation map in (a) and (b), respectively. **e)** Representative orientations of the host (blue triangle) and lamellae (yellow triangle) depicted in (a) of the {0001}, {11$\bar{2}$0}, and {10$\bar{1}$1} planes. **f)** Representative orientations (green, blue, and pink triangles) of the three different crystallographic domains depicted in (b) of the {0001}, {11$\bar{2}$0}, and {10$\bar{1}$1} planes.

Fig. 6 EBSD data of ilmenite aggregate within sample CT827a, Zipplingen. **a)** All Euler orientation map. Note the larger grains with concave grain boundaries indicated by the three arrows as well as the region strongly enriched in TiO_2 displayed by the white line. **b)** GROD map displaying the angular deviation from the average grain orientation. Note the grains with internal misorientation and irregular grain boundaries indicated by the white arrows. **(c-e)** Ilmenite pole

figures of the {0001}, {11$\bar{2}$0}, and {10$\bar{1}$1} planes of **c)** grains <5 µm, **d)** grains 5 – 10 µm, **e)** grains >10 µm. **f)** Orientation of all grains with GROD coloring as displayed in (b). Blue circles indicate that the enclosed orientation data is mostly derived from grains with low internal misorientation, whereas red circles indicate that the enclosed orientation data is mostly derived from grains with relatively high internal misorientation.

Fig. 7 Ferropseudobrookite in Fe-Ti oxide aggregates, sample CT827a, Zipplingen. **a, b)** Fe-Ti-oxide aggregate with magnetite (Mag) at the rim and within the (devitrified) matrix (gl); BSE images. Yellow rectangles in (b) indicate the close-ups in (c), (d), and (e). **c, d)** Ferropseudobrookite (Fpb) along a fracture within the ilmenite aggregate, where sphene (Spn) is locally present. Note symplectic intergrowth of ferropseudobrookite and ilmenite (Ilm) as well as rutile grains [Rt; dark grey in (c) and white in (d)] along ilmenite grain boundaries at the top of the images; BSE and reflected single plane-polarized light, respectively. **e)** Close-up of rutile (Rt) along ilmenite (Ilm) boundaries, as well as a symplectic intergrowth of ilmenite and ferropseudobrookite (Fpb) at the contact to the (devitrified) matrix (gl), where (sub-)euhedral magnetite grains (Mag) also occur; BSE image. **f)** Traces of (sub-)euhedral magnetite grains (Mag) within the (devitrified) matrix (gl) in close distance to an intergrowth of ilmenite (Ilm) and porous ferropseudobrookite (Fpb).

Fig. 8 EBSD and EDS data of ilmenite and ferropseudobrookite aggregates, sample CT827, Zipplingen. **a)** Reflected light micrograph of a Fe-Ti-oxide aggregate. The red rectangle depicts the area displayed in (b-d, g, h). **b)** Phase distribution map of ilmenite (Ilm; red),

ferropseudobrookite (Fpb; green), sphene (Spn; light blue), magnetite (Mag; dark blue), and rutile (Rt; yellow). **c)** Ilmenite orientation map (inverse pole figure of z-direction). **d)** Ferropseudobrookite orientation map (inverse pole figure of z-direction). **e)** Pole figures of the {0001}, {11$\bar{2}$0}, and {10$\bar{1}$1} planes of ilmenite displayed in (c). **f)** Pole figures of the {100}, {010}, and {001} planes of ferropseudobrookite displayed in (d). **g)** Manganese (Mn) and **h)** magnesium (Mg) distribution within the Fe-Ti-oxide aggregate.

Fig. 9 BSE images of Fe-Ti-oxide microfabrics within suevite sample R20-16A from Aumühle. **a)** Coarse ilmenite grain (Ilm) within a cryptocrystalline matrix (cr) containing vesicles (vs). The yellow rectangle depicts the area in (b). **b)** Ilmenite (Ilm) with foam structure. **c)** Fe-Ti-oxide (fto) reaction fabric within a vesicle-bearing (vs) cryptocrystalline matrix (cr). The yellow rectangle depicts the area in (d). **d)** Ilmenite with a rim of pseudorutile (Prt). Remnants of ilmenite in the bottom right are mostly covered by pseudorutile. **e)** Former ilmenite grain transformed almost completely to pseudorutile (Prt) with preferentially oriented pores/cracks and remnants of foam-structured ilmenite (Ilm). **f)** Foam-structured ilmenite (Ilm) with a finer-scaled ilmenite rim (Ilm rim) embedded in a cryptocrystalline matrix (cr).

Fig. 10 High-pressure phase transformations of $FeTiO_3$. **a)** Phase transformations during loading and unloading of $FeTiO_3$ with their respective symmetries, space group numbers (No.), as well as crystallographic lattice parameters a, b, and c. **b)** Group theoretical analysis of the symmetry conversion (blue dashed lines) of ilmenite, wangdaodeite, and liuite with the respective Bain-correspondence matrix. Note that all symmetries derive from the cubic perovskite

supersymmetry. Point groups and their respective order are in orange. The red dashed line indicates reconstructive positional shifts of the phase transitions. The generation of transformation twins occurs from the transformation of liuite to wangdaodite.

Fig. 11 Summary and interpretations of this study. Pressure (P; green), temperature (T; red), and relative oxygen fugacity (fO_2; blue) conditions as a function of time based on the observed characteristic Fe-Ti-oxide microfabrics. **I)** Foam-structured ilmenite (Ilm). **II)** Ferropseudobrookite (Fpb; dark grey) along a fracture within a Fe-Ti-oxide aggregate. Note that rarely observed armalcolite (Arm) likely formed from Fpb. **III)** Rutile (Rt) along grain boundaries of ilmenite (Ilm). **IV)** Ilmenite (Ilm) aggregate containing rutile (Rt) and with a rim enriched in Fe (Fe↑). **V)** (Sub-)euhedral magnetite (Mag). **VI)** Pseudorutile (Prt) as rim around grains of ilmenite aggregates (Ilm). (bI) – (bV) sample CT827a and (bVI) sample R20-16A. Note that reactions as a function of temperature (red arrows) are always coupled to oxygen fugacity reaction (blue arrows) conditions and vice versa, in contrast to the high-pressure reaction (green arrows). The dashed lines represent pressure, temperature, and oxygen fugacity regimes in which the corresponding reactions take place, except for reaction IV, which presumably takes place up to the ferropseudobrookite stability field (1140°C). BSE images (bI)-(bIV), (bVI) and SE image (bV). Pressure conditions after Leinenweber et al. (1991); temperature and oxygen fugacity conditions after Lindsley (1965), Keil et al. (1970), Tuthill and Sato (1970), Taylor et al. (1972), Mitchell et al. (1982), Kuroda and Mitchell (1983), Gupta et al. (1991), and Sargeant et al. (2020).

Tab. 1 EMP data (wt.%) of ilmenite (Ilm), ferropseudobrookite (Fpb), and armalcolite (Arm) from sample CT827a (Figs. 4, 8) as well as ilmenite and pseudorutile (Prt) from sample R20-16A

1088 (Fig. 9c, d). Note that the detection limit in ppm is given in brackets for a concentration below
1089 0.004 wt.% and/or a not detectable (n.d.) component (*=data as Fe_2O_3). The deviation of the total
1090 wt.% can be explained for ilmenite due to the presence of a Fe_2O_3 component, which binds more
1091 oxygen and thus would increase the calculated total. Porosity of ferropseudobrookite(-armalcolite
1092 solid solution) (Fig. 7c-f) leads to a decrease in the total wt.%, whereas in pseudorutile, the
1093 presence of water and/or hydroxyl groups decreases the total wt.%.

1094

Phase	Fig.	FeO / Fe_2O_3*	TiO_2	MnO	MgO	SiO_2	Al_2O_3	Na_2O	CaO	K_2O	Total
Ilm	4 (core)	41.35	51.86	3.80	1.55	0.08	n.d. (253)	0.03	0.05	n.d. (239)	98.72
Ilm	4 (core)	41.52	51.91	3.91	1.55	0.10	n.d. (253)	0.01	0.05	0.02	99.07
Ilm	4 (core)	41.41	51.91	3.90	1.54	0.07	n.d. (253)	n.d. (370)	0.06	n.d. (239)	98.88
Ilm	4 (rim)	40.86	51.89	3.65	2.08	0.09	0.02	0.02	0.06	(249)	98.67
Ilm	4 (rim)	41.88	51.27	3.90	1.47	0.06	0.09	0.02	0.09	0.01	98.80
Ilm	4 (rim)	41.44	51.61	4.01	1.60	0.10	0.11	0.02	0.07	(240)	98.96
Ilm	8	41.83	50.79	5.68	0.41	0.06	n.d. (239)	0.03	0.04	0.01	98.87
Ilm	8	41.42	51.28	5.49	0.43	0.10	(239)	0.02	0.05	0.01	98.85
Ilm	8	42.14	50.68	5.74	0.40	0.07	n.d. (239)	0.03	0.04	(242)	99.11
Fpb	8	33.89	59.69	1.86	0.37	0.75	0.10	0.02	0.56	0.02	97.31
Fpb	8	34.47	59.39	2.20	0.21	0.55	0.11	0.01	0.10	0.02	97.07
Fpb	8	34.31	60.33	1.72	0.40	0.45	0.14	n.d. (379)	0.12	0.01	97.50
Arm	8	30.54	57.72	0.93	2.61	3.17	0.82	0.10	0.29	0.16	96.45
Arm	8	29.83	59.98	1.20	2.05	1.35	0.32	0.04	0.20	0.04	95.09
Arm	8	31.08	60.30	1.32	1.64	2.51	0.30	0.09	0.33	0.06	97.76
Ilm	9c, d	50.74	44.46	1.70	0.52	0.07	n.d. (242)	0.02	0.03	(249)	97.56
Ilm	9c, d	46.74	48.66	1.94	0.66	0.04	0.01	0.03	0.06	0.03	98.16
Ilm	9c, d	48.56	46.64	1.70	0.69	0.08	n.d. (242)	0.04	0.03	n.d. (241)	97.78
Prt	9c, d	41.93*	52.84	1.06	0.11	0.29	n.d. (242)	0.01	0.04	0.01	96.33
Prt	9c, d	41.96*	52.53	0.81	0.07	0.33	n.d. (242)	0.02	0.04	(233)	95.79
Prt	9c, d	41.42*	52.80	0.80	0.08	0.37	n.d. (242)	0.01	0.06	n.d. (233)	95.56

1095

1096 **Tab. 2** Investigated rim and core of aggregates of Fe- and/or Ti-bearing phases (Ilm = ilmenite;
1097 Mag = magnetite; Rt = rutile; Spn = sphene; Fpb = ferropseudobrookite; Arm = armalcolite)
1098 within sample CT827a. The lowercase numbers indicate their occurrence in %.

Size [µm]	Rim phase(s)	Core phase(s)
160 x 80	Ilm_{50}, Arm_{50}	Fpb_{60}, Ilm_{35}, $Spn_{<5}$, $Rt_{<5}$
120 x 100	Mag	Ilm_{85}, Fpb_{10}, $Spn_{<5}$, $Rt_{<5}$
160 x 70	Mag	Ilm_{85}, $Spn_{<15}$, $Rt_{<1}$

Size [µm]	Rim phase(s)	Core phase(s)
100 x 40	Ilm_{50}, Rt_{50}	Ilm
70 x 50	Mag	$Ilm_{>95}$, $Rt_{<5}$
100 x 30	-	$Ilm_{>95}$, $Rt_{<5}$

This is the peer-reviewed, final accepted version for American Mineralogist, published by the Mineralogical Society of America.
The published version is subject to change. Cite as Authors (Year) Title. American Mineralogist, in press.
DOI: https://doi.org/10.2138/am-2023-8985. http://www.minsocam.org/

170 x 50	Ilm_{80}, Mag_{20}	Ilm_{95}, Rt_{5}
160 x 50	-	Ilm
120 x 80	Fpb	Ilm_{85}, $Rt_{<10}$, $Spn_{<5}$
100 x 90	Ilm	Ilm_{95}, Rt_{5}
120 x 60	$Mag_{>95}$, $Ilm_{<5}$	$Ilm_{>95}$, $Rt_{<5}$
100 x 60	Mag	$Ilm_{>95}$, $Rt_{<5}$
80 x 70	Mag	Ilm_{85}, Fpb_{10}, $Mag_{<5}$, $Rt_{<5}$
80 x 60	-	$Ilm_{>95}$, $Rt_{<5}$
70 x 60	-	$Ilm_{>95}$, $Rt_{<5}$
60 x 50	-	$Ilm_{>95}$, $Rt_{<5}$
140 x 20	-	$Ilm_{>95}$, $Rt_{<5}$
100 x 25	Mag	Ilm_{95}, Rt_{5}
70 x 30	Mag	Ilm_{95}, Rt_{5}
40 x 30	Mag	Ilm_{85}, Rt_{15}
40 x 30	-	Spn_{50}, Mag_{20}, Ilm_{15}, Rt_{15}
40 x 20	-	Ilm
10 x 10	Mag	$Ilm_{>95}$, $Rt_{<5}$

Tab. 3 Investigated rim and core of aggregates of Fe- and/or Ti-bearing phases (Ilm = ilmenite; Prt = pseudorutile; Rt = rutile) within sample R20-16A. The lowercase numbers indicate their occurrence in % (* = sub-aggregates of fractured ilmenite).

Size [µm]	**Rim phase(s)**	**Core phase(s)**
180 x 120	Ilm	Ilm_{95}, Prt_{5}
220 x 70	Ilm	Ilm
70 x 30	-	Ilm
50 x 20	Ilm	$Ilm_{>95}$, $Prt_{<5}$
40 x 25	Ilm	Ilm
40 x 20	-	$Ilm_{>95}$, $Rt_{<5}$
20 x 10	-	Ilm_{95}, Prt_{5}
15 x 10	-	$Ilm_{>95}$, $Prt_{<5}$
*140 x 50	-	Ilm
*40 x 15	-	Ilm
*30 x 20	-	Ilm
*10 x 5	-	Ilm

Supplementary Data

Tab. S1 EMP data [wt.%] of profile (step size ≈1 µm) from core (#1) to rim (#29) depicted in Figure 3g, h with the at.%-ratio of iron and titanium (Fe/Ti). Note that Fe/Ti increases towards the aggregate's rim and #1-#4 correspond to rutile with varying amounts of FeO. The detection limit in ppm is given in brackets for either a concentration below 0.004 wt.% or a not detectable

This is the peer-reviewed, final accepted version for American Mineralogist, published by the Mineralogical Society of America.
The published version is subject to change. Cite as Authors (Year) Title. American Mineralogist, in press.
DOI: https://doi.org/10.2138/am-2023-8985. http://www.minsocam.org/

(n.d.) component. The deviation of the total wt.% can be explained due to the presence of Fe_2O_3, which binds more oxygen and thus would increase the calculated total.

#	FeO	TiO_2	MnO	MgO	SiO_2	Al_2O_3	Na_2O	CaO	K_2O	Total	Fe/Ti
1	32.16	61.35	2.17	2.72	0.24	(249)	0.01	0.06	0.01	98.72	0.58
2	7.13	86.93	0.64	0.59	0.26	(251)	0.02	0.08	0.01	95.67	0.09
3	2.57	95.05	0.20	0.17	0.34	n.d. (251)	0.01	0.07	0.02	98.44	0.03
4	12.35	86.26	0.62	1.00	1.30	0.03	0.01	0.08	0.02	101.71	0.16
5	35.43	59.39	2.14	2.93	0.93	0.09	0.02	0.12	0.01	101.09	0.66
6	36.66	57.19	2.39	3.20	0.47	0.02	0.01	0.08	n.d. (249)	100.05	0.71
7	35.76	55.36	2.43	3.27	0.80	0.05	0.02	0.09	0.02	97.81	0.72
8	29.87	67.05	1.74	2.32	0.63	0.04	n.d. (260)	0.09	(247)	101.75	0.50
9	32.45	58.88	2.31	2.87	0.94	0.06	0.05	0.11	0.02	97.73	0.61
10	18.29	74.21	1.40	1.81	0.76	0.09	0.05	0.13	0.02	96.76	0.27
11	23.87	69.43	1.62	2.07	0.46	0.07	0.02	0.09	(248)	97.65	0.38
12	37.60	55.63	2.16	2.82	0.69	0.10	0.01	0.14	0.02	99.19	0.75
13	39.98	52.47	2.43	3.41	0.27	0.09	n.d. (380)	0.10	0.02	98.78	0.85
14	39.53	52.66	2.49	3.47	0.23	0.07	n.d. (380)	0.09	0.02	98.56	0.83
15	39.52	52.82	2.52	3.47	0.22	0.11	n.d. (380)	0.11	0.01	98.80	0.83
16	39.42	52.68	2.58	3.53	0.27	0.10	0.03	0.09	0.01	98.70	0.83
17	39.56	52.42	2.49	3.53	0.26	0.10	0.01	0.11	n.d. (244)	98.48	0.84
18	39.57	52.39	2.45	3.45	0.27	0.11	0.01	0.10	0.01	98.38	0.84
19	39.59	52.40	2.43	3.51	0.31	0.13	0.03	0.08	0.01	98.54	0.84
20	39.84	52.11	2.40	3.37	0.31	0.14	0.03	0.10	0.01	98.34	0.85
21	39.94	51.97	2.45	3.35	0.25	0.14	0.01	0.10	(238)	98.22	0.85
22	39.95	51.98	2.40	3.46	0.29	0.14	0.02	0.13	0.01	98.43	0.85
23	40.21	51.90	2.36	3.36	0.33	0.18	0.02	0.10	0.02	98.51	0.86
24	39.96	51.44	2.29	3.27	0.72	0.23	0.02	0.16	0.02	98.14	0.86
25	40.39	50.87	2.33	3.38	0.40	0.24	n.d. (367)	0.16	0.02	97.81	0.88
26	40.64	50.83	2.27	3.36	0.27	0.24	0.01	0.15	0.02	97.81	0.89
27	40.85	50.50	2.18	3.31	0.36	0.25	0.01	0.18	0.03	97.68	0.90
28	41.24	49.38	2.03	3.22	0.46	0.33	n.d. (373)	0.20	0.04	96.92	0.93
29	41.44	45.28	1.99	3.01	7.75	1.75	0.22	0.29	0.28	102.03	1.02

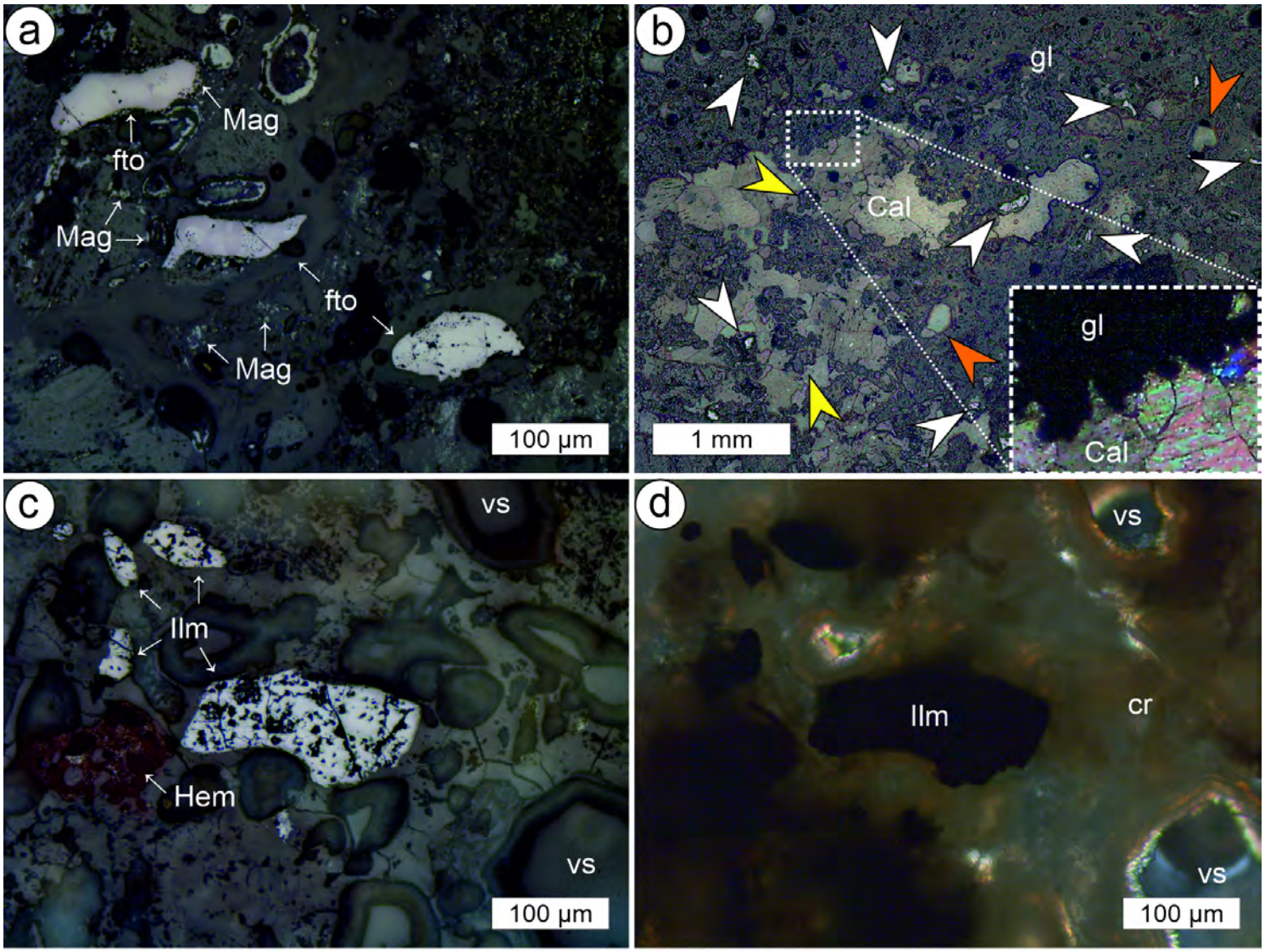
a
Mag
fto
Mag
fto
Mag
100 µm
b
gl
Cal
gl
Cal
1 mm
c
vs
Ilm
Hem
vs
100 µm
d
vs
Ilm
cr
vs
100 µm

Figure 1

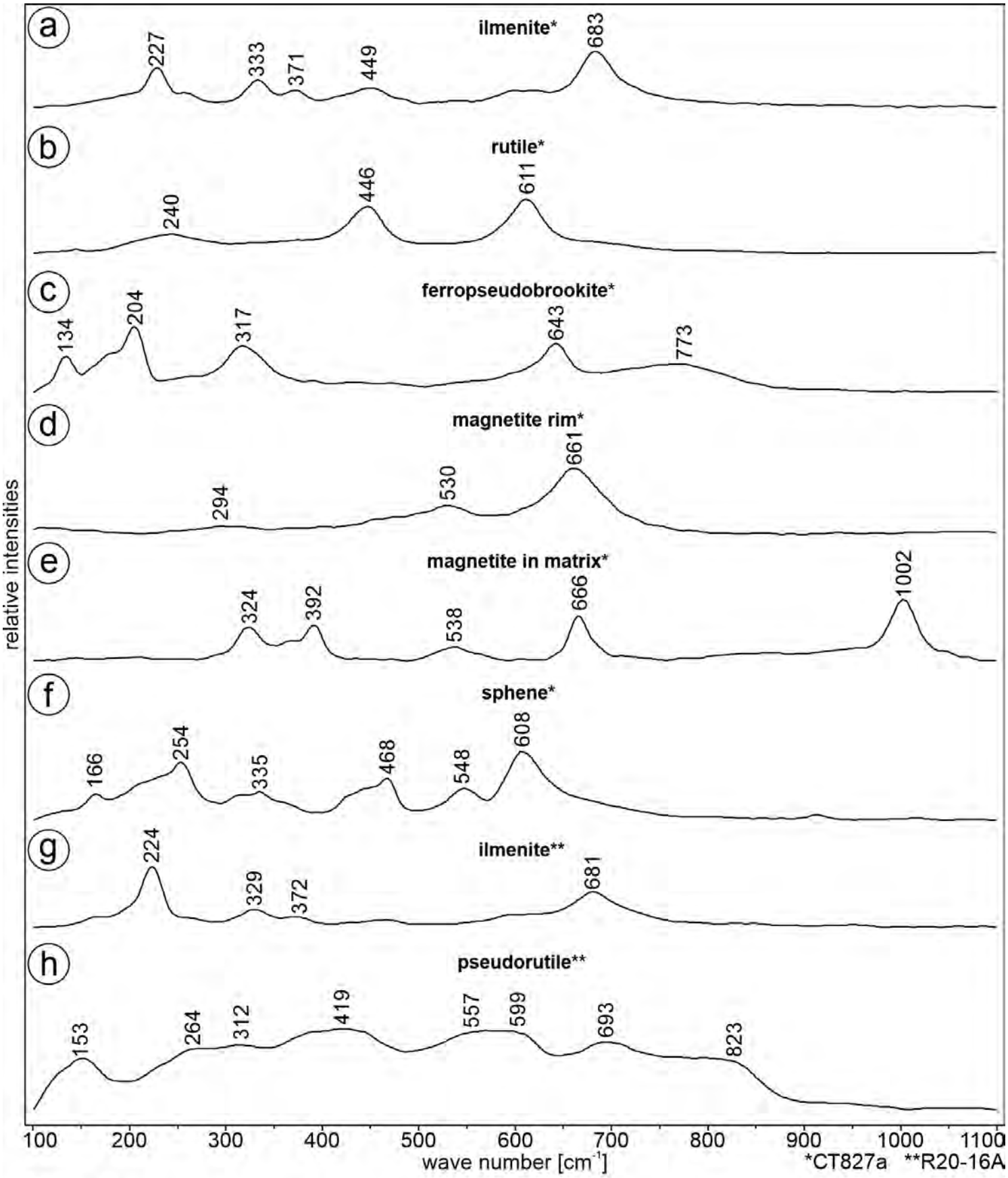
a
ilmenite*
227
333
371
449
683
b
rutile*
240
446
611
c
ferropseudobrookite*
134
204
317
643
773
d
magnetite rim*
294
530
661
e
magnetite in matrix*
324
392
538
666
1002
f
sphene*
166
254
335
468
548
608
g
ilmenite**
224
329
372
681
h
pseudorutile**
153
264
312
419
557
599
693
823
relative intensities
100
200
300
400
500
600
700
800
900
1000
1100
wave number [cm-1]
*CT827a **R20-16A

Figure 2

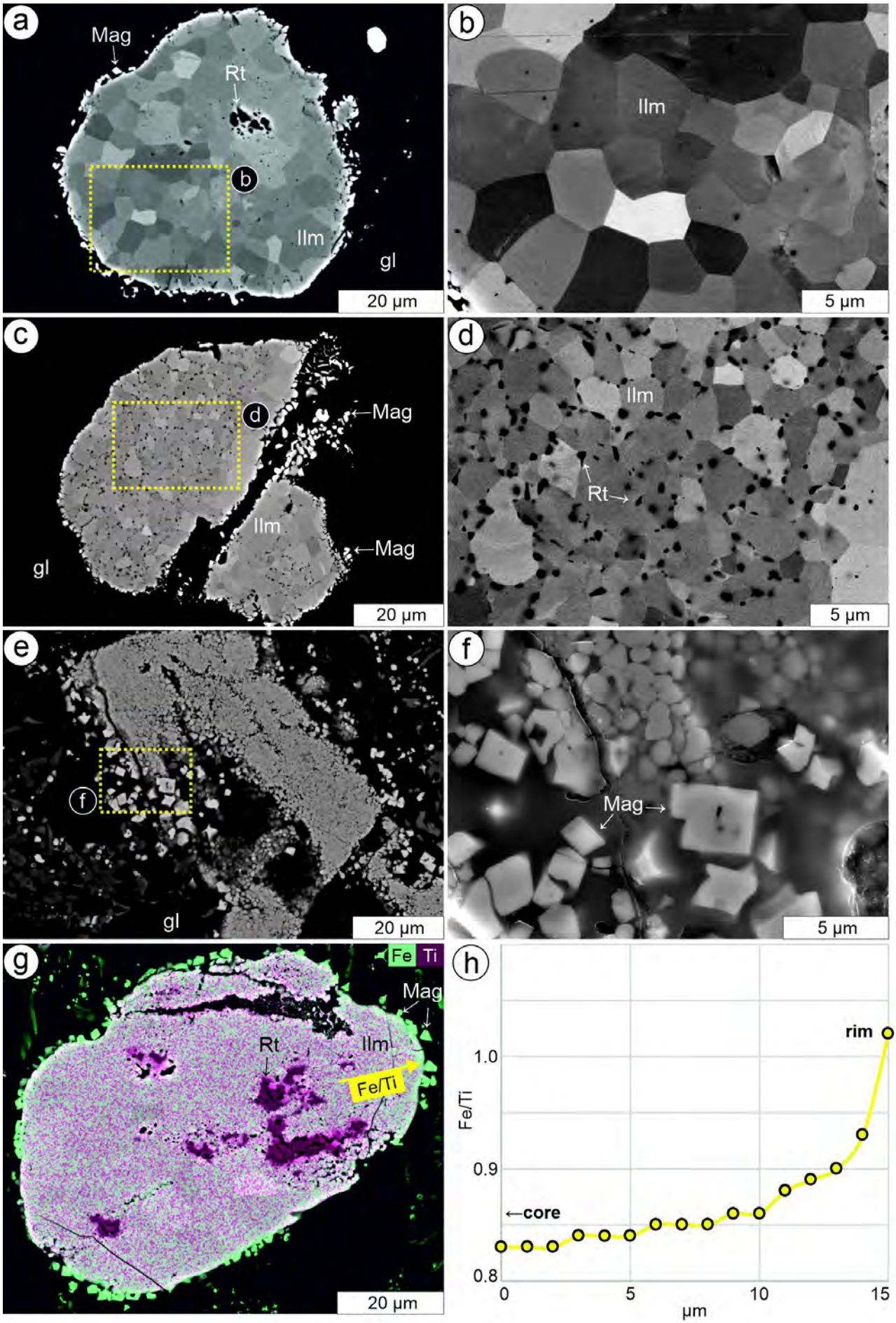
a
Mag
Rt
b
Ilm
gl
20 µm
b
Ilm
5 µm
c
d
←Mag
Ilm
←Mag
gl
20 µm
d
Ilm
Rt→
5 µm
e
f
gl
20 µm
f
Mag→
5 µm
g
Fe
Ti
Mag
Rt
Ilm
Fe/Ti
20 µm
h
rim
1.0
0.9
0.8
Fe/Ti
←core
0
5
10
15
µm

Figure 3

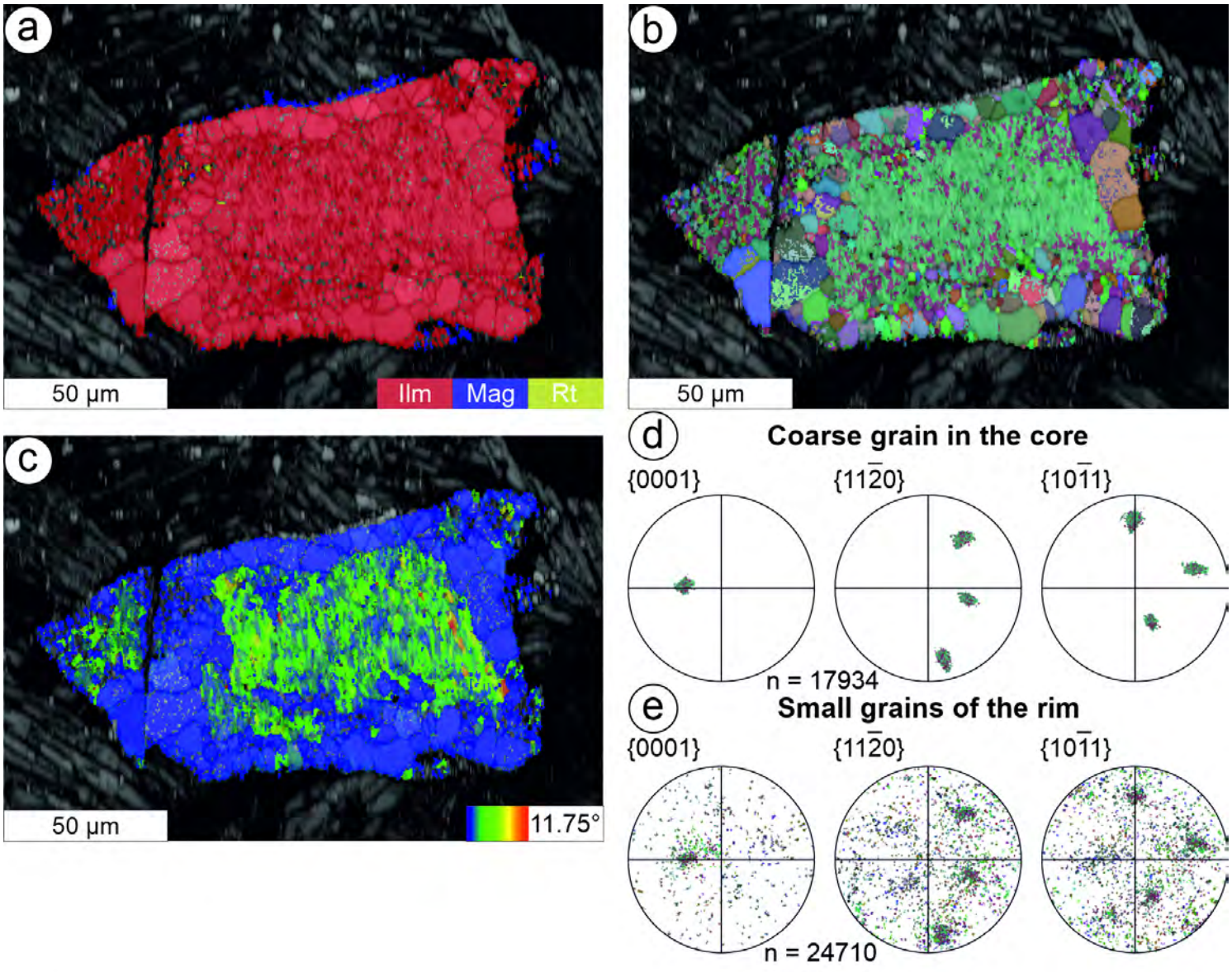
a
50 µm
Ilm
Mag
Rt
b
50 µm
c
50 µm
11.75°
d
Coarse grain in the core
{0001}
{11$\bar{2}$0}
{10$\bar{1}$1}
n = 17934
e
Small grains of the rim
{0001}
{11$\bar{2}$0}
{10$\bar{1}$1}
n = 24710

Figure 4

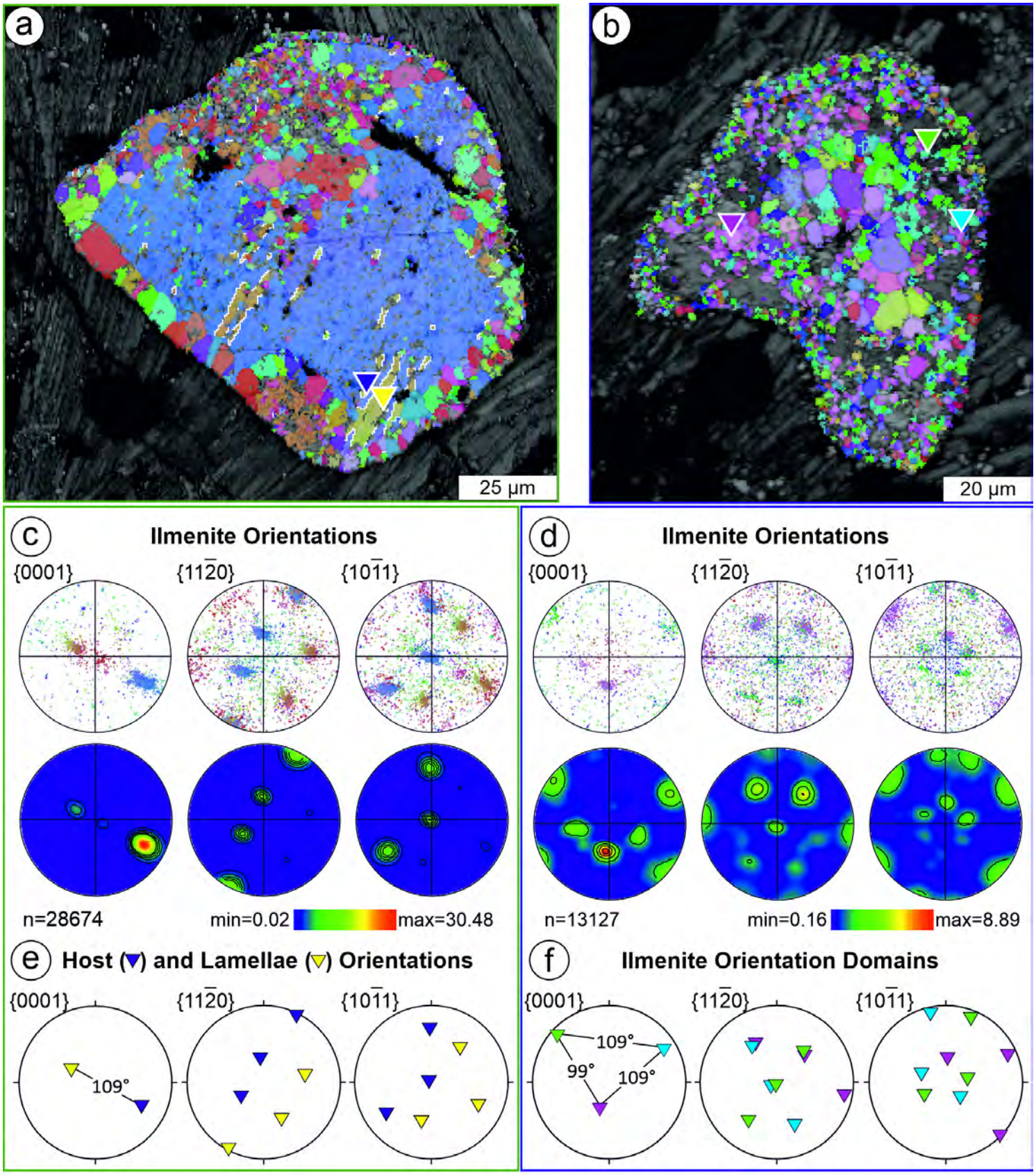
a
25 µm
b
20 µm
c
Ilmenite Orientations
{0001}
{11$\bar{2}$0}
{10$\bar{1}$1}
n=28674
min=0.02
max=30.48
d
Ilmenite Orientations
{0001}
{11$\bar{2}$0}
{10$\bar{1}$1}
n=13127
min=0.16
max=8.89
e
Host (▼) and Lamellae (▽) Orientations
{0001}
{11$\bar{2}$0}
{10$\bar{1}$1}
109°
f
Ilmenite Orientation Domains
{0001}
{11$\bar{2}$0}
{10$\bar{1}$1}
109°
99°
109°

Figure 5

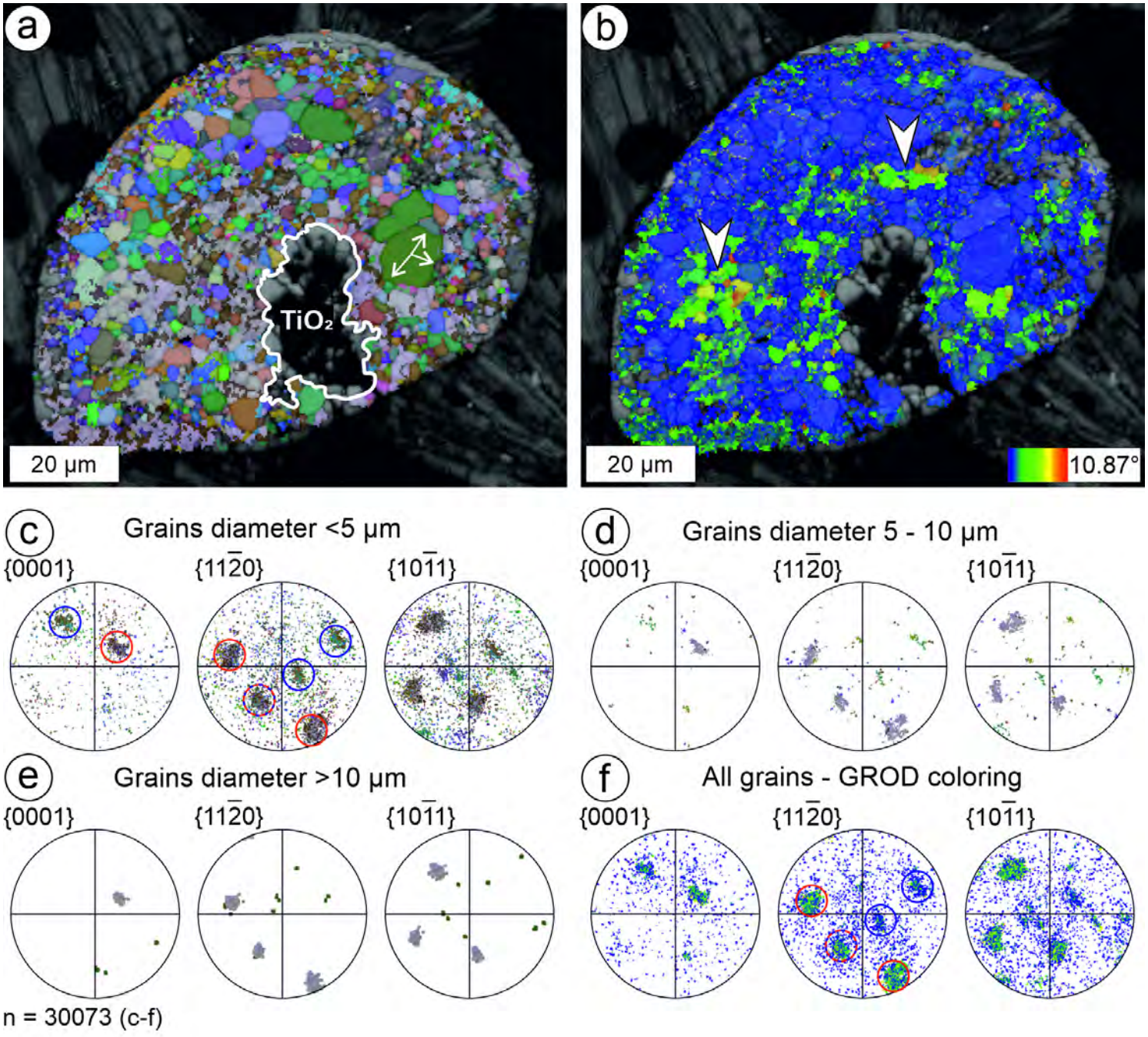
a
b
TiO2
20 µm
20 µm
10.87°
c
Grains diameter <5 µm
{0001}
{11$\bar{2}$0}
{10$\bar{1}$1}
d
Grains diameter 5 - 10 µm
{0001}
{11$\bar{2}$0}
{10$\bar{1}$1}
e
Grains diameter >10 µm
{0001}
{11$\bar{2}$0}
{10$\bar{1}$1}
f
All grains - GROD coloring
{0001}
{11$\bar{2}$0}
{10$\bar{1}$1}
n = 30073 (c-f)

Figure 6

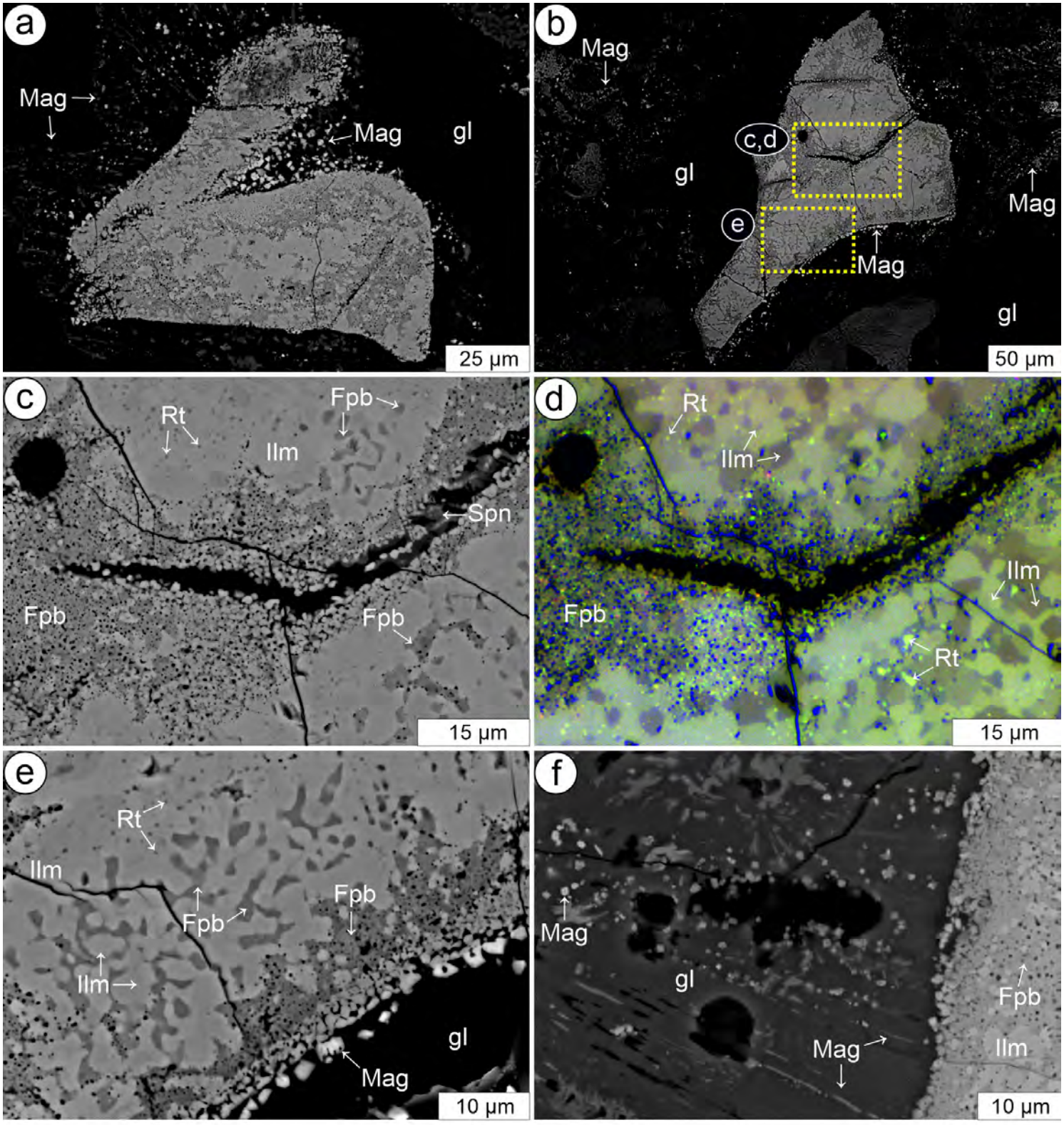
a
Mag
Mag
gl
25 µm
b
Mag
c,d
gl
e
Mag
Mag
gl
50 µm
c
Rt
Fpb
Ilm
Spn
Fpb
Fpb
15 µm
d
Rt
Ilm
Ilm
Fpb
Rt
15 µm
e
Rt
Ilm
Fpb
Fpb
Ilm
gl
Mag
10 µm
f
Mag
gl
Fpb
Mag
Ilm
10 µm

Figure 7

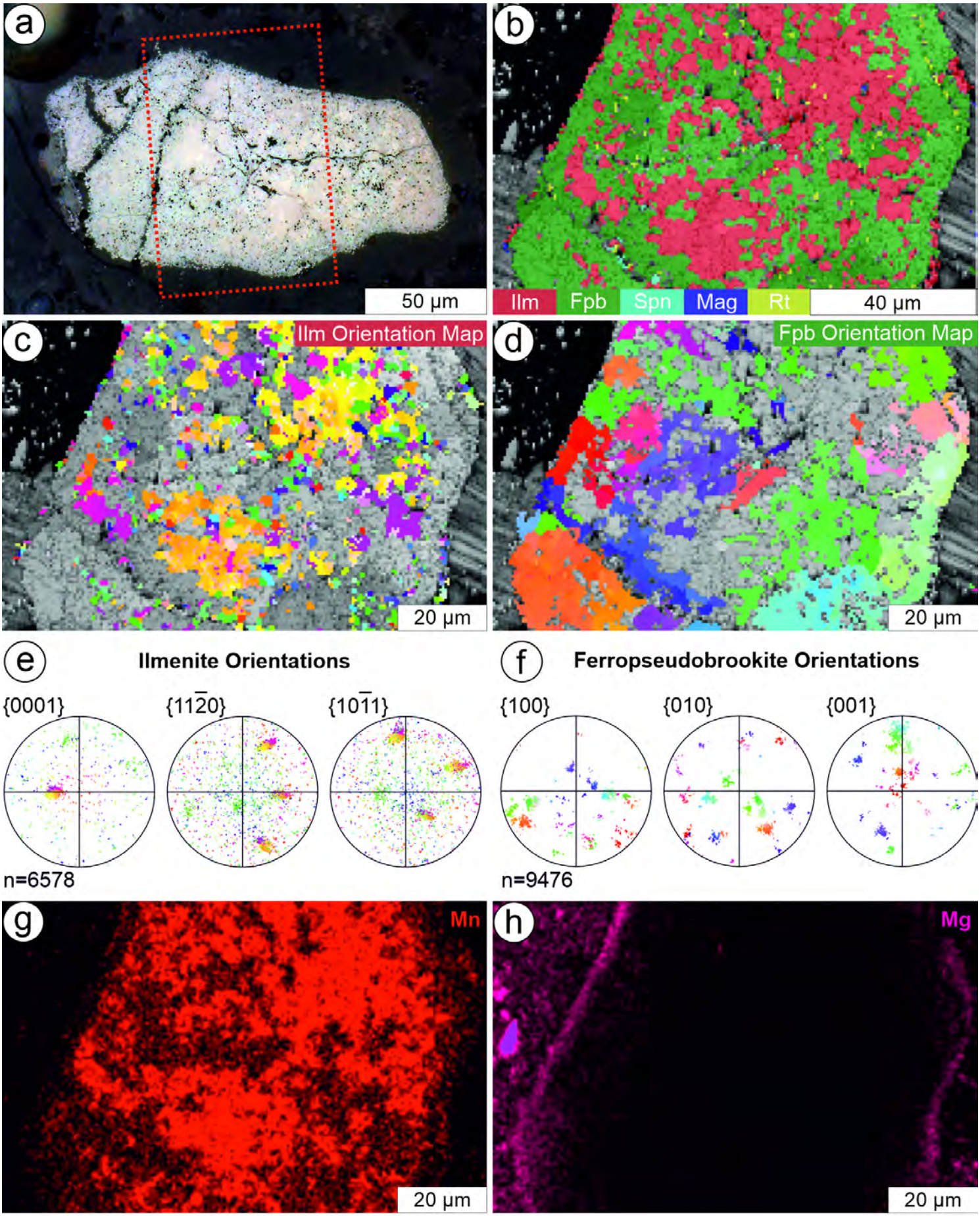
a
50 µm
b
Ilm
Fpb
Spn
Mag
Rt
40 µm
c
Ilm Orientation Map
20 µm
d
Fpb Orientation Map
20 µm
e
Ilmenite Orientations
{0001}
{11$\bar{2}$0}
{10$\bar{1}$1}
n=6578
f
Ferropseudobrookite Orientations
{100}
{010}
{001}
n=9476
g
Mn
20 µm
h
Mg
20 µm

Figure 8

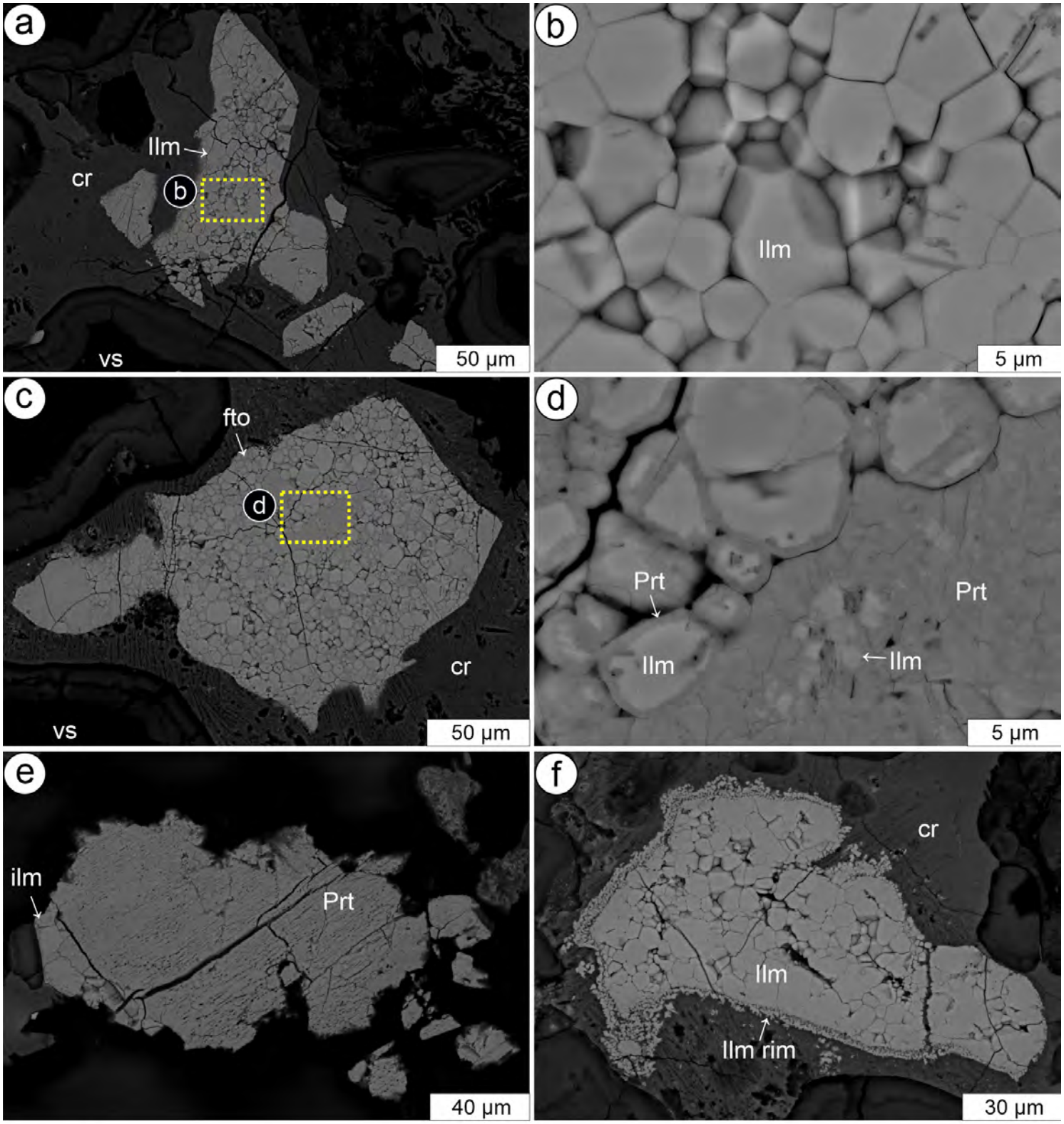
a
Ilm
cr
b
vs
50 µm
b
Ilm
5 µm
c
fto
d
cr
vs
50 µm
d
Prt
Prt
Ilm
Ilm
5 µm
e
ilm
Prt
40 µm
f
cr
Ilm
Ilm rim
30 µm

Figure 9

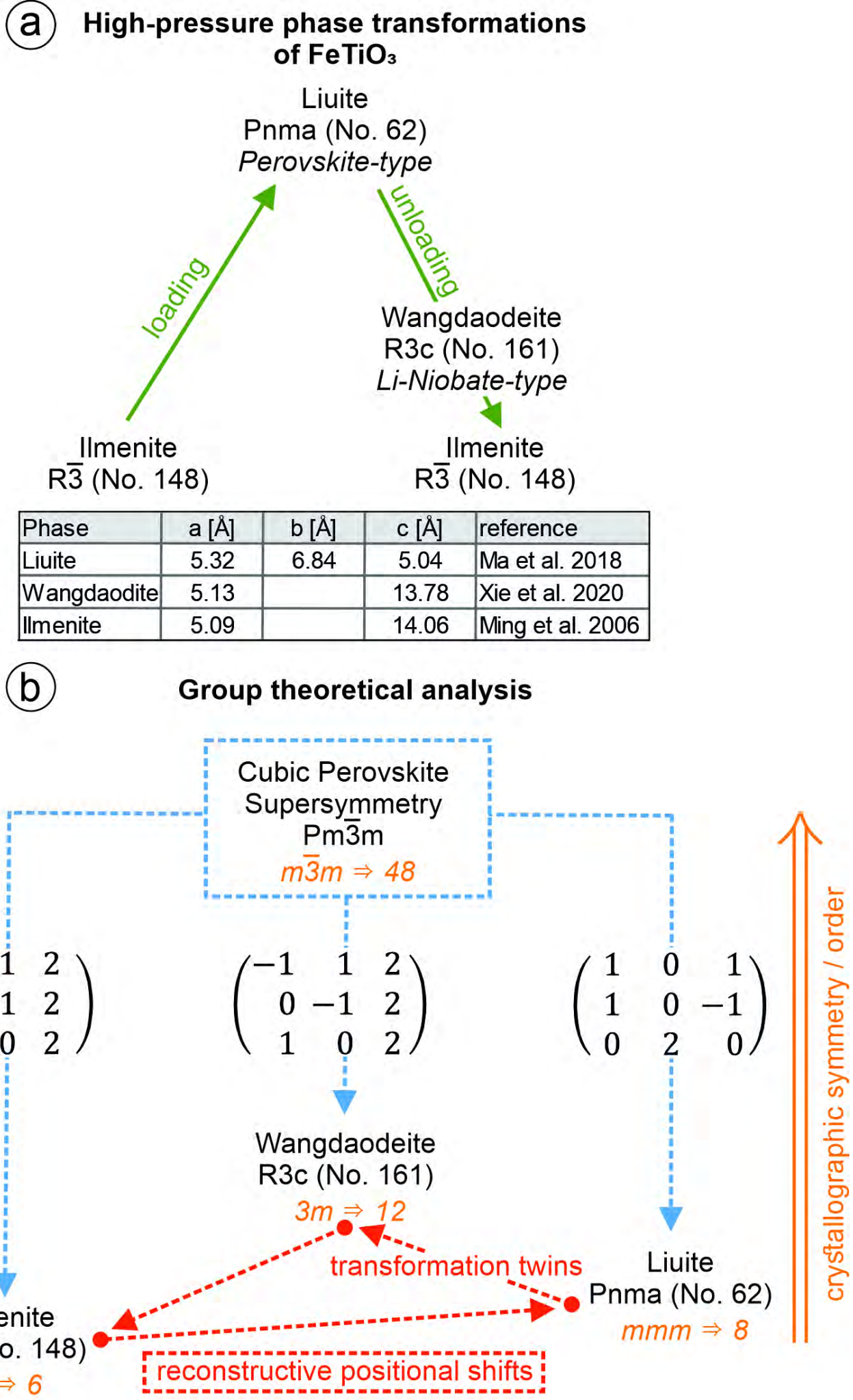

Phase	a [Å]	b [Å]	c [Å]	reference
Liuite	5.32	6.84	5.04	Ma et al. 2018
Wangdaodite	5.13		13.78	Xie et al. 2020
Ilmenite	5.09		14.06	Ming et al. 2006

Figure 10

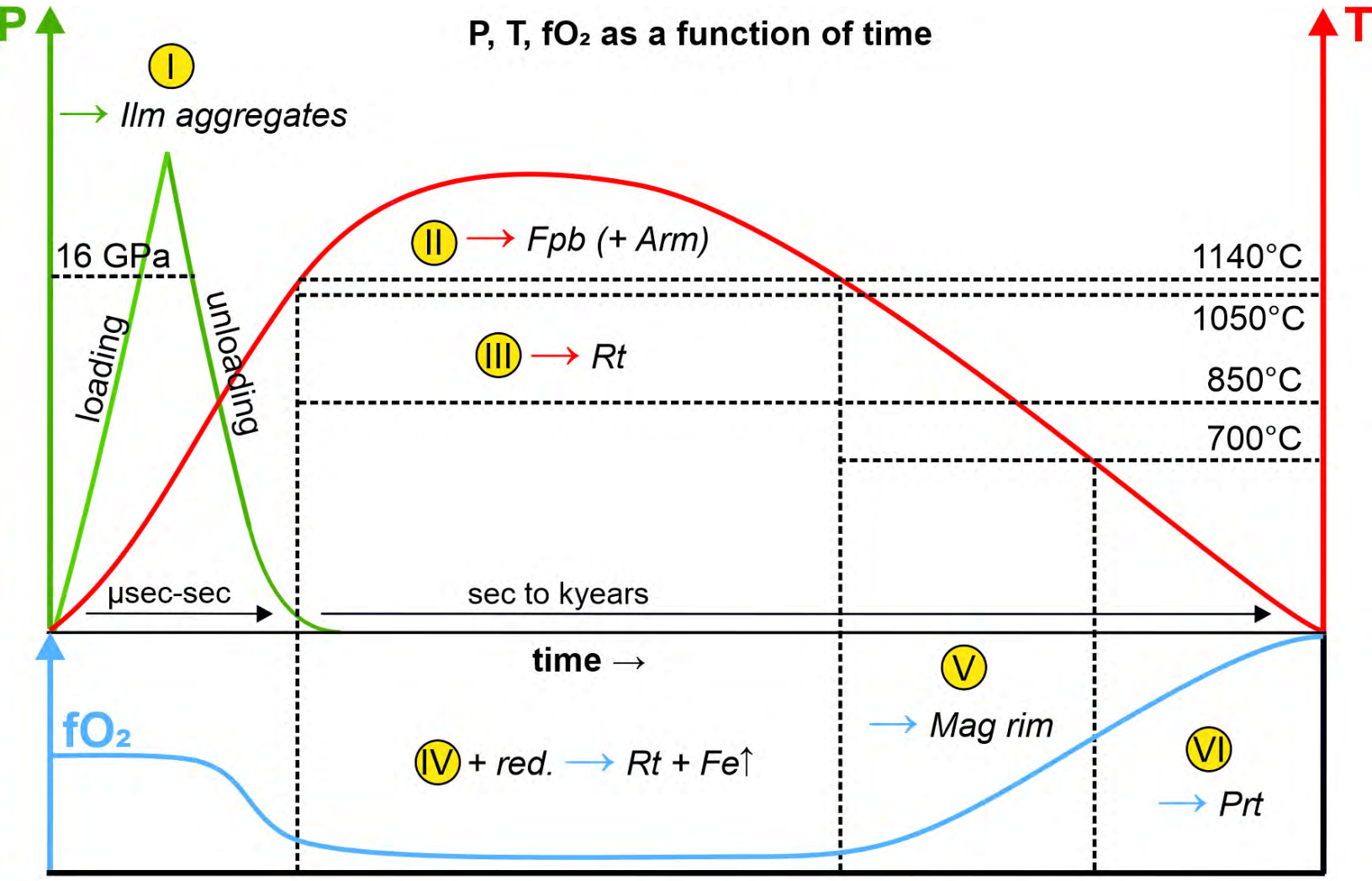

Characteristic Fe-Ti-oxide microfabrics

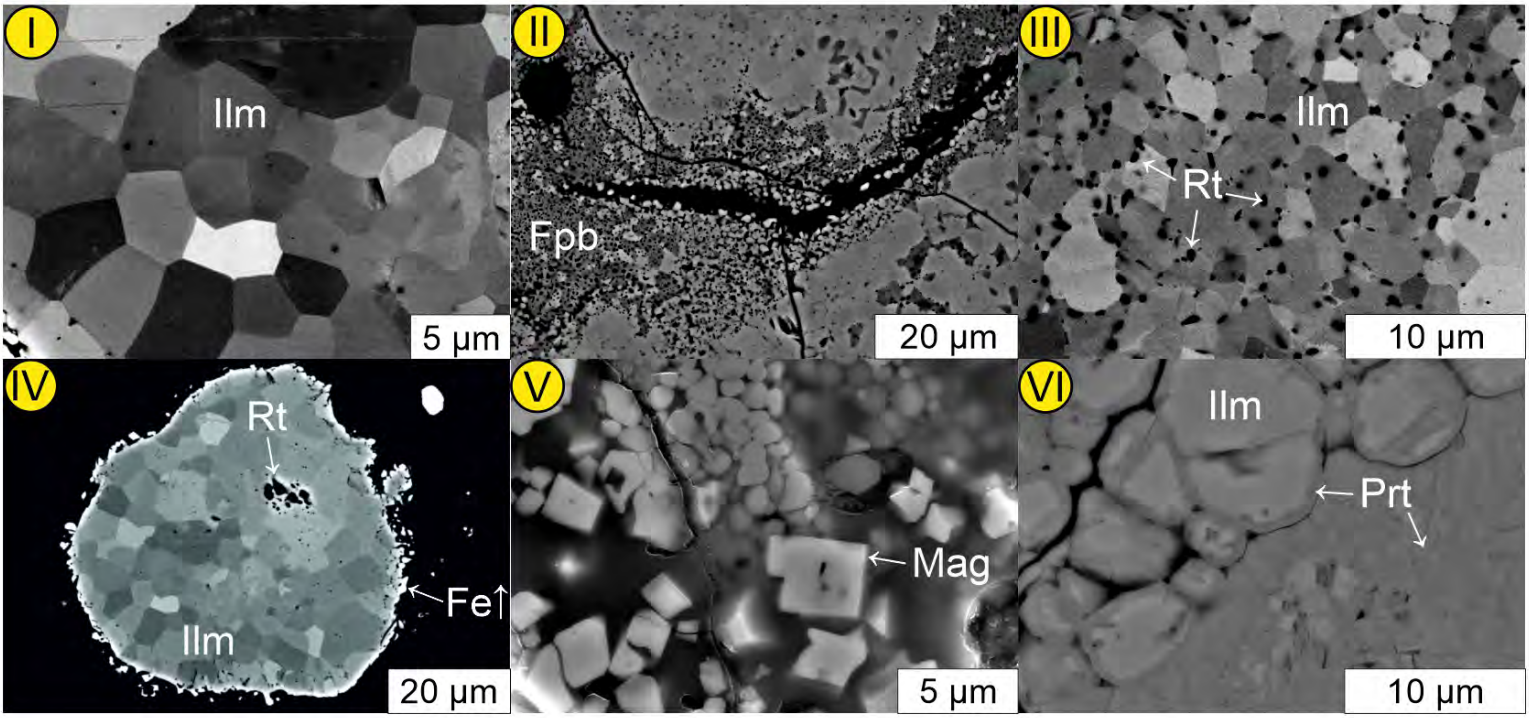

Figure 11